AGU PUBLICATIONS

Geophysical Research Letters

RESEARCH LETTER
10.1002/2017GL076437

Key Points:
- The influence of Southern Ocean surface buoyancy forcing on the AMOC depth is tested in a comprehensive climate model
- Applying LGM surface forcing in the Southern Ocean shoals the AMOC only about half as much as applying LGM surface forcing globally
- Southern Ocean diapycnal mixing makes the AMOC depth sensitive to both Southern Ocean and North Atlantic surface buoyancy forcing

Supporting Information:
- Supporting Information S1

Correspondence to:
S. Sun,
shantong@ucsd.edu

Citation:
Sun, S., Eisenman, I., & Stewart, A. (2018). Does Southern Ocean surface forcing shape the global ocean overturning circulation? *Geophysical Research Letters*, *45*, 2413–2423. https://doi.org/10.1002/2017GL076437

Received 16 NOV 2017
Accepted 8 FEB 2018
Accepted article online 12 FEB 2018
Published online 9 MAR 2018

Does Southern Ocean Surface Forcing Shape the Global Ocean Overturning Circulation?

Shantong Sun[1], Ian Eisenman[1], and Andrew L. Stewart[2]

[1]Scripps Institution of Oceanography, University of California, San Diego, La Jolla, CA, USA, [2]Department of Atmospheric and Oceanic Sciences, University of California, Los Angeles, CA, USA

Abstract Paleoclimate proxy data suggest that the Atlantic Meridional Overturning Circulation (AMOC) was shallower at the Last Glacial Maximum (LGM) than its preindustrial (PI) depth. Previous studies have suggested that this shoaling necessarily accompanies Antarctic sea ice expansion at the LGM. Here the influence of Southern Ocean surface forcing on the AMOC depth is investigated using ocean-only simulations from a state-of-the-art climate model with surface forcing specified from the output of previous coupled PI and LGM simulations. In contrast to previous expectations, we find that applying LGM surface forcing in the Southern Ocean and PI surface forcing elsewhere causes the AMOC to shoal only about half as much as when LGM surface forcing is applied globally. We show that this occurs because diapycnal mixing renders the Southern Ocean overturning circulation more diabatic than previously assumed, which diminishes the influence of Southern Ocean surface buoyancy forcing on the depth of the AMOC.

1. Introduction

In the modern climate, the deep Atlantic Ocean below 2,000 m is filled with Antarctic Bottom Water (AABW) as well as North Atlantic Deep Water (NADW) (Talley, 2013). At the Last Glacial Maximum (LGM) ~21,000 years ago, however, paleoclimate proxy data suggest that NADW was absent below 2,000 m depth with an expanded volume occupied by AABW (e.g., Burke et al., 2015; Lund et al., 2011). This suggests that the Atlantic Meridional Overturning Circulation (AMOC), which is the Atlantic branch of the global ocean overturning circulation that spreads NADW southward from the North Atlantic, was shallower at the LGM compared with modern conditions. Attempts to simulate this difference with climate models have yielded mixed results (e.g., Muglia & Schmittner, 2015; Otto-Bliesner et al., 2007). For example, in the Paleoclimate Model Intercomparison Project Phase 3, all models except for the Community Climate System Model version 4 (CCSM4) simulated a deeper AMOC in simulations of the LGM compared to simulations of the preindustrial (PI) climate (Muglia & Schmittner, 2015).

Because the deep ocean is the largest carbon reservoir in the land-atmosphere-ocean system (Sarmiento & Gruber, 2002), rearrangement of deep water masses could lead to substantial variations in the atmospheric CO_2 concentration (Sigman et al., 2010), which was approximately 80 ppm lower at the LGM than during the PI period (Monnin et al., 2001). Using an Earth System Model of Intermediate Complexity, Brovkin et al. (2007) suggested that expansion of the carbon-rich AABW at the LGM can draw down the atmospheric CO_2 level by 10–20 ppm. Furthermore, because mixing is most vigorous below 2,000 m, the shoaling of the water mass boundary between AABW and NADW at the LGM has been suggested to have substantially reduced the mixing between the two water masses (Ferrari et al., 2014), which is a major source of leakage for abyssal carbon in the modern ocean (Lund et al., 2011). This reduced vertical mixing between AABW and NADW may have further enhanced the ability of the abyssal ocean to trap carbon and contribute to the lower atmospheric CO_2 levels at the LGM (Lund et al., 2011).

Based on analyses of model simulations and paleoclimate proxy data from the LGM, Ferrari et al. (2014) suggested that the shallower AMOC at the LGM is dynamically linked to changes in the surface buoyancy forcing in the Southern Ocean. This idea is further supported by a pair of idealized modeling studies, which suggested that a broader region of surface buoyancy loss in the Southern Ocean, associated with the expansion of Antarctic sea ice, leads to a shallower AMOC at the LGM (Burke et al., 2015; Watson et al., 2015). Both studies are based on an idealized, two-dimensional, residual mean model of the global ocean overturning circulation (Nikurashin & Vallis, 2011, 2012). In this two-dimensional view, the overturning circulation is composed

of two overturning circulation cells: an upper cell (i.e., the AMOC), which is associated with the southward transport of NADW and occupies roughly the upper 3,000 m in the modern Atlantic Ocean, and a lower cell that spreads AABW northward from the Southern Ocean. The two overturning circulation cells diverge at the Southern Ocean surface where the surface buoyancy forcing changes sign.

Ferrari et al. (2014) suggested that the depth of the AMOC can thereby be inferred from the surface buoyancy flux in the Southern Ocean under two approximations: (1) fixed isopycnal slope in the Southern Ocean and (2) adiabatic circulation in the upper Southern Ocean so that the residual mean overturning circulation follows isopycnal contours. They predicted that a 500 km equatorward expansion of sea ice, which is consistent with paleoclimate proxy reconstructions of the LGM (e.g., Gersonde et al., 2003, 2005), would expand the buoyancy loss region equatorward in the Southern Ocean and imply shoaling of the AMOC by 500 m.

Though conceptually illuminating, the applicability of the geometric argument of Ferrari et al. (2014) to the real ocean remains uncertain. Their approximation that the isopycnal slope in the Southern Ocean is insensitive to surface forcing perturbations is only qualitatively supported in observations (Böning et al., 2008) and models (Gent & Danabasoglu, 2011; Viebahn & Eden, 2010). More importantly, observations suggest that there is substantial diapycnal mixing over rough topography in the Southern Ocean (e.g., Mashayek et al., 2017; Naveira Garabato et al., 2004; Whalen et al., 2012; Wu et al., 2011), which is at odds with the adiabatic approximation for the Southern Ocean circulation. In the present study, three simulations that were carried out with the ocean component of a state-of-the-art climate model are analyzed to investigate the extent to which changes in Southern Ocean surface buoyancy forcing alone can explain the shoaling of the AMOC at the LGM.

2. Description of Simulations

Three simulations were carried out with a configuration of the National Center for Atmospheric Research Community Earth System Model version 1.1.2 (CESM1.1.2) in which only the ocean is active, with the atmosphere, sea ice, and land runoff specified using output from previous coupled CCSM4 simulations of the PI (Gent et al., 2011) and LGM climates (Brady et al., 2013). The ocean component of CESM1.1.2 (Danabasoglu et al., 2012), which is identical to CCSM4, is run with a horizontal resolution of nominally 1°, with unresolved eddies parameterized using the Gent-McWilliams scheme (Gent & Mcwilliams, 1990). There are 60 vertical levels with thicknesses ranging from 10 m at the surface to 250 m at the ocean bottom. Vertical convection is represented by the nonlocal K-profile parameterization (Large et al., 1994), in which diapycnal diffusivity is parameterized to account for processes including convective instability, internal wave breaking, double diffusion, and tidally driven mixing. Except in regions of deep convection or in the boundary layer, the dominant term in the diapycnal diffusivity is due to the parameterized tidally driven mixing, which scales inversely with the density stratification (Jayne, 2009).

The three ocean-only simulations share the same model configuration, including the same PI ocean bathymetry, except that they have different surface forcing: one control run (called PI) is forced by PI surface conditions, a second control run (called LGM) is forced by LGM surface conditions, and a test run (called Test) is forced by LGM surface conditions south of 40°S and PI surface conditions north of 30°S, with a linear transition from LGM to PI conditions in the region between 40°S and 30°S. These simulations were originally carried out as part of a previous study (Sun et al., 2016). Further details about the model setup and forcing can be found in Text S1 in the supporting information, which draws on a number of previous studies (Brady et al., 2013; Gent et al., 2011; Gent & Danabasoglu, 2011; Gent & Mcwilliams, 1990; Large et al., 1994; Marzocchi & Jansen, 2017; Mazloff et al., 2010; Sun et al., 2016; Zhang et al., 2013).

All three simulations are identically initialized from the end of the coupled PI run. As a result, the PI ocean-only simulation equilibrates most rapidly, and it is run for 510 years. The Test and LGM simulations are run for 1,020 and 1,440 years, respectively. At the end of the simulations, all three runs have approximately equilibrated (see Text S1 in the supporting information). Unless otherwise noted, the analyses in this study use 5 day mean model output during the last 20 years of each model run.

The zonal mean wind stress forcing and wind stress curl are plotted in Figure S1 in the supporting information. The westerly wind stress forcing in the Southern Ocean is shifted equatorward without much change in intensity at the LGM compared with PI (cf. Brady et al., 2013). Note that this is in contrast to an LGM simulation with an earlier version of the coupled model (Otto-Bliesner et al., 2006). Figure S2 shows the zonal

mean surface buoyancy flux in the Southern Ocean in the three ocean-only simulations. Close to Antarctica, the buoyancy flux is negative mainly due to brine rejection from sea ice formation. The LGM simulation has a colder global ocean temperature than the Test simulation, which appears to lead to more frazil ice formation in the Southern Ocean and hence stronger buoyancy loss close to Antarctica. Consequently, the latitude where surface buoyancy flux changes sign differs slightly between the LGM and Test simulations: the region of negative buoyancy flux extends approximately 3.4° and 2.5° latitude farther equatorward in the LGM and Test simulations, respectively, compared to the PI simulation.

3. Simulation Results

3.1. Meridional Overturning Circulation Streamfunction

Here we calculate the Meridional Overturning Circulation (MOC) streamfunction ψ on σ_2 coordinates as follows:

$$\psi(y,\sigma_2) = -\frac{1}{T}\int_0^T \int_{x_w}^{x_e} \int_{z_{\text{bot}}}^0 v_r(x,y,z,t)\mathcal{H}\left(\sigma_2'(x,y,z,t) - \sigma_2\right) \mathrm{d}z\,\mathrm{d}x\,\mathrm{d}t, \tag{1}$$

where σ_2 is the potential density referenced to 2,000 dbar, σ_2' is the σ_2 field reported by the model, x is the longitudinal displacement, y is the latitudinal displacement, z is depth with z_{bot} the depth of the ocean bottom, $T = 20$ years is the averaging period, $\mathcal{H}$ is the Heaviside step function, and v_r is the total meridional velocity that includes both the Eulerian mean flow and the eddy-bolus contribution due to the parameterized mesoscale and submesoscale eddies. In the Atlantic basin, ψ is integrated from the western boundary (x_w) to the eastern boundary (x_e). In the Southern Ocean, we integrate zonally around the globe along each latitude circle. We calculate the MOC streamfunction ψ in equation (1) using 5 day mean model output, which is short enough to resolve much of the temporal variability that contributes to the overturning circulation (cf. Ballarotta et al., 2013).

The MOC streamfunction on σ_2 coordinates can be mapped to depth coordinates using the mean depth of each isopycnal. Here we define the mean depth of an isopycnal $\hat{z}(y,\sigma_2)$ implicitly via

$$\int_{x_w}^{x^e} \int_{z_{\text{bot}}}^{\hat{z}(y,\sigma_2)} \mathrm{d}x\,\mathrm{d}z = \frac{1}{T}\int_0^T \int_{x_w}^{x_e} \int_{z_{\text{bot}}}^0 \mathcal{H}\left(\sigma_2(x,y,z,t) - \sigma_2'\right) \mathrm{d}x\,\mathrm{d}z\,\mathrm{d}t, \tag{2}$$

following Nurser and Lee (2004); that is, the total cross-sectional area below $\hat{z}$ at latitude y is equal to the cross-sectional area of fluid denser than σ_2. We use this definition instead of the time and zonal mean isopycal depth because of the unstable density stratification in regions where convection occurs (Nurser & Lee, 2004). Therefore, the MOC streamfunction on depth coordinates, $\hat{\psi}$, can be written as $\hat{\psi}(y,z) = \hat{\psi}(y,\hat{z}(y,\sigma_2)) = \psi(y,\sigma_2)$, using $z = \hat{z}(y,\sigma_2)$. We use the mean isopycnal depth $\hat{z}$ to similarly define the mean potential density on depth coordinates, $\hat{\sigma}_2(y,z)$, such that $\hat{\sigma}_2 = \sigma_2$ at $z = \hat{z}(y,\sigma_2)$.

The MOC streamfunction in the three simulations is plotted on depth coordinates in Figure 1 (and on σ_2 coordinates in Figure S4). For purely adiabatic flow in steady state, $\hat{\psi}$ is constant along $\hat{\sigma}_2$ contours. Hence, the deviation of $\hat{\psi}$ from $\hat{\sigma}_2$ contours in Figure 1 (and equivalently deviations from horizontal contours in Figure S4) in the Southern Ocean implies the presence of diapycnal mixing. Qualitatively similar features of flow crossing isopycnals in the Southern Ocean also occur in the 1/6° Southern Ocean State Estimate (Mazloff et al., 2013, their Figure 1), a 1/10° CESM simulation (Bishop et al., 2016, their Figure 8), and a 1/10° CCSM3.5 simulation (Newsom et al., 2016, their Figure 7).

We quantify the diapycnal mixing in the Southern Ocean that occurs in the three simulations analyzed here in Text S3 in the supporting information, which draws on a number of previous studies (Griffies et al., 2000; Hill et al., 2012; Jayne, 2009; Munk, 1966; Newsom et al., 2016; Sun et al., 2016; Walin, 1982; Waterhouse et al., 2014; Watson et al., 2013). Specifically, we compare the MOC streamfunction at 30°S with the water mass transformation due to surface buoyancy forcing, following the framework of Walin (1982). We find that diapycnal mixing plays a dominant role in Southern Ocean water mass transformation. This finding is similar to the results of Newsom et al. (2016).

However, because the isopycnals vary both longitudinally and temporarily due to both standing eddies (cf. Tréguier et al., 2007) and the time-varying buoyancy forcing in the Southern Ocean, diapycnal mixing that occurs in some regions of Figure 1 could be caused by mixed layer eddies (Karsten et al., 2002; Marshall et al., 1999) or water mass transformation due to surface buoyancy forcing (see Figure S2). We construct an upper

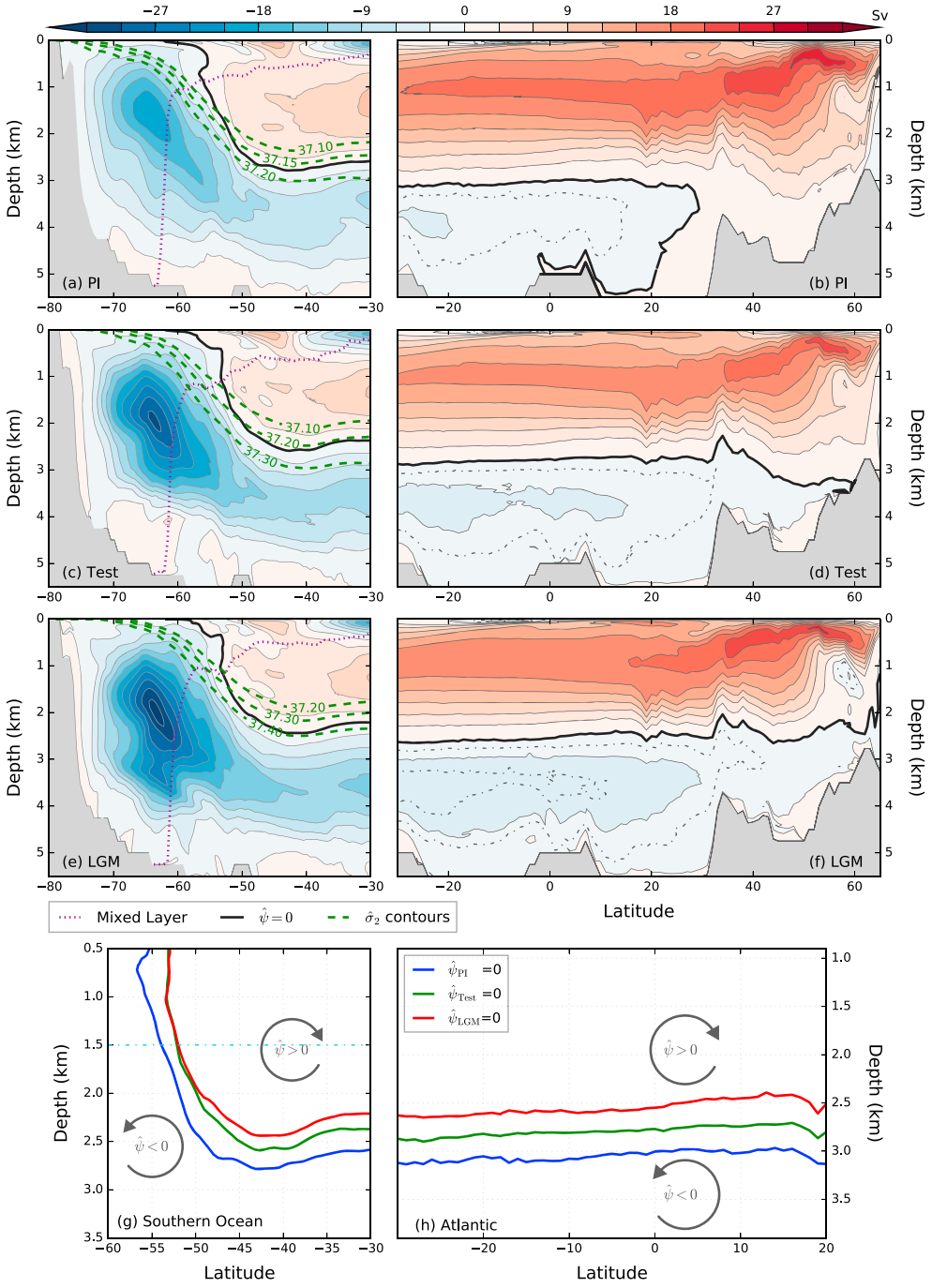

Figure 1. Overturning circulation streamfunction mapped to depth coordinates in (a, c, and e) the Southern Ocean and (b, d, and f) the Atlantic Ocean. In each panel, the streamline that separates the upper and lower overturning circulation cells ($\hat{\psi} = 0$) is plotted as a thick black contour. Three isopycnals near this streamline in the Southern Ocean are plotted as green dashed lines. The maximum depth of the surface mixed layer (MML) is plotted as a purple dotted line. The contour interval is 3 Sv; additional contours at −4.5 Sv and −1.5 Sv are also included in the Atlantic as dash-dotted lines. To remove noise at the grid scale, the overturning circulation streamfunction is smoothed using a five-point (~ 2.5° latitude) running mean along isopycnal contours; the unsmoothed version is included in the supporting information (Figure S5). (g, h) The Meridional Overturning Circulation depth, defined as the depth of the streamline $\hat{\psi} = 0$, is plotted for comparison among the three simulations. The cyan dash-dotted line at 1.5 km depth in the Southern Ocean indicates the approximate MML in the plotted latitude range. Note that the axis ranges in these panels differ from the panels above: the vertical ranges are adjusted to focus on the differences between the simulations, and the horizontal range in the Atlantic ends at 20°N due to the zero streamline not extending north of this latitude in the preindustrial (PI) simulation. LGM = Last Glacial Maximum.

bound on the density classes impacted directly by mixed layer processes and surface forcing by defining the maximum depth of the mixed layer (MML) (cf. Iudicone et al., 2008; Marshall et al., 1999). Specifically, we define the MML as the densest isopycnal at each latitude that ever occurs within the mixed layer at any longitude and any time during the 20 year averaging period (purple line in Figure S4), which is then mapped to depth coordinates (purple dotted line in Figure 1). Hence, isopycnals below the MML are not affected by mixed layer dynamics or surface transformation. Note that the MML is generally deeper than the mixed layer depth as reported directly in the CESM model output, where it is defined as the shallowest depth where the local, interpolated vertical buoyancy gradient matches the maximum buoyancy gradient within the full column (Large et al., 1997). Due to the occurrence of deep convection close to Antarctica in the model, the MML reaches the seafloor south of 60° S (Figure 1).

3.2. MOC Depth and Shoaling of the AMOC

In this study, we define the MOC depth as the depth of the streamline $\hat{\psi} = 0$ (thick solid line in Figure 1) that separates the upper and lower overturning circulation cells. In the PI run, the AMOC extends approximately over the upper 3,000 m. This is roughly consistent with modern observations (Lozier, 2012). The AMOC is approximately 500 m shallower in the LGM run, which is forced by the LGM surface conditions globally (Figure 1h). This shoaling in the LGM run compared with the PI run approximately matches the depth change predicted by Ferrari et al. (2014). Note that it is smaller than the 1,000 m shoaling suggested by some paleoproxy reconstructions (e.g., Lund et al., 2011), and it is approximately 200 m larger than in the coupled CCSM4 simulations (cf. Muglia & Schmittner, 2015), although the deep ocean circulation in the coupled CCSM4 LGM simulation does not appear to be fully equilibrated (Marzocchi & Jansen, 2017).

In the Test run, which has LGM surface conditions only in the Southern Ocean and PI surface conditions elsewhere, the geometric argument of Ferrari et al. (2014) predicts that the AMOC depth should be similar to the LGM run. However, in contrast with this expectation, the AMOC in the Test run is only approximately 250 m shallower than in the PI run, which is half as much shoaling as in the LGM run. The AMOC depth changes in these simulations appear to be largely explained by the MOC depth differences in the Southern Ocean (Figure S6), consistent with the approximately uniform changes in the AMOC depth throughout the Atlantic basin between the three simulations (Figure 1h). In contrast with Jansen and Nadeau (2016), who attributed differences in the AMOC depth to changes in the abyssal stratification that occur due to surface buoyancy loss in the Southern Ocean, here the abyssal stratification in the Test run is similar to the LGM run (Sun et al., 2016).

Note that we use σ_2 in this analysis rather than neutral density, even though adiabatic motion occurs on local neutral surface and hence neutral density is better conserved (McDougall, 1987). This choice is made because the calculation of neutral density involves a prelabeled global reference data set that is derived from observations (Jackett & McDougall, 1997), which is not available for the LGM and Test simulations. For this and other reasons, the σ_2 coordinate is often used in studies of the overturning circulation in climate model simulations (e.g., Bishop et al., 2016; Gent & Danabasoglu, 2011; Newsom et al., 2016). To test the sensitivity of the results to this choice, we also perform the above calculations using a different potential density coordinate (σ_1), and the results appear not to be substantially different. For example, the difference in the AMOC depth at 30°S between the Test and LGM runs calculated on σ_1 coordinates is 262 m, which is very close to the value of 250 m calculated on σ_2 coordinates (cf. Figure 1h). We also examine the influence of model equilibrium on our results in Text S1 in the supporting information. The results suggest that the model is approximately equilibrated and that the difference in AMOC depth between the Test and LGM simulations is substantially larger than any adjustments that would likely occur if the simulations were run longer.

4. Interpretation of the MOC Depth Changes

The Southern Ocean MOC depth in the Test run is approximately the same as in the LGM run throughout the upper 1,500 m (Figure 1g), consistent with the two runs having similar surface buoyancy forcing (Figure S2). Below 1,500 m, however, the Test run diverges from the LGM run in Figure 1g. This can be caused by the small changes in the isopycnal slope (see Figures S7 and S8, as well as Text S2, which draws on a number of previous studies, Böning et al., 2008; Ferrari et al., 2014; Gent & Danabasoglu, 2011; Viebahn & Eden, 2010; Wolfe & Cessi, 2010), by the presence of diapycnal mixing (see Figure S9 and Text S3), or by both. In this section, we derive a scaling relationship that we use to attribute the contributions to the differences in AMOC depth between the simulations that arise due to differences in surface forcing, isopycnal slope, diapycnal mixing, and isopycnal upwelling.

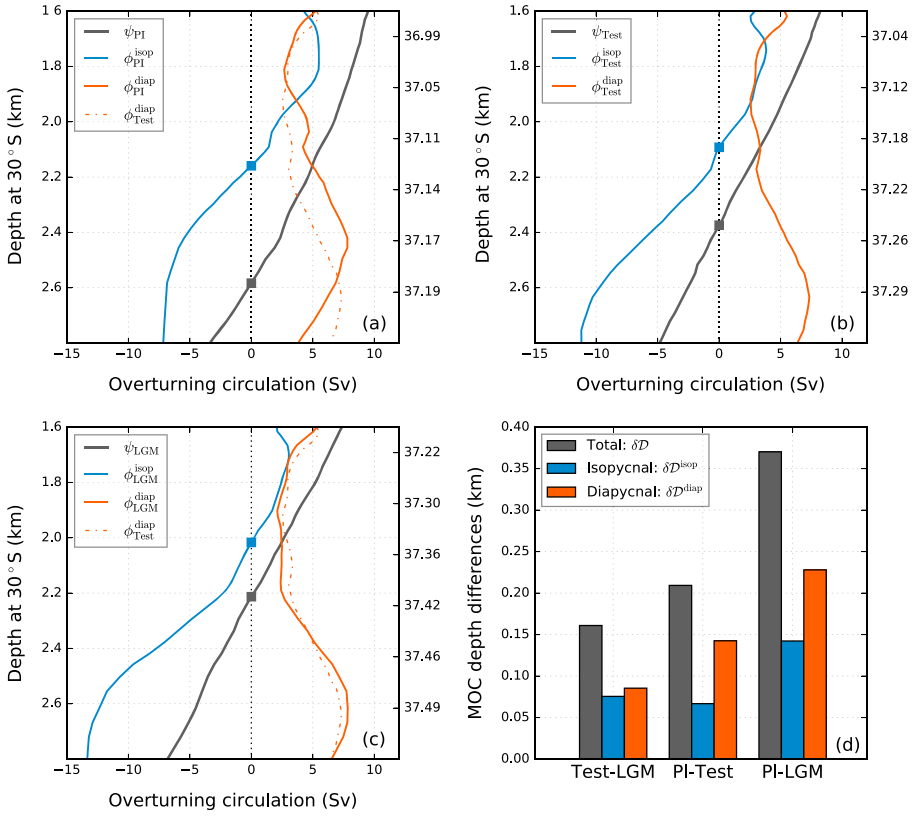

Figure 2. (a–c) Meridional Overturning Circulation (MOC) streamfunction components $\psi(30°\mathrm{S}, \sigma_2)$, $\phi^{\mathrm{isop}}(\sigma_2)$, and $\phi^{\mathrm{diap}}(\sigma_2)$, mapped to depth coordinates using the mean isopycnal depth at 30°S (see details in section 4), with corresponding potential densities σ_2 labeled on the right axis, for each simulation. The three solid curves in each panel can be interpreted as follows: the black line shows the simulated overturning circulation streamfunction at 30°S, the blue line (ϕ^{isop}) shows the MOC streamfunction that would occur at 30°S if the circulation were purely adiabatic below z_{ref} in the Southern Ocean, and the red line (ϕ^{diap}) shows the difference between ϕ and ϕ^{isop}. Hence, ϕ^{diap} quantifies the along-isopycnal change in the MOC streamfunction due to diapycnal mixing below $z_{\mathrm{ref}} = -1.5$ km in the Southern Ocean. The ϕ^{diap} curve in the Test run is repeated for comparison in panels (a) and (c) as a dash-dotted red line. The MOC depths corresponding to $\psi(30°\mathrm{S}, \sigma_2)$ and ϕ^{isop} are indicated in each panel by the blue and black squares, respectively. (d) Contribution to the inter-simulation differences in the MOC depths (black) due to changes in shapes of isopycnals and surface forcing (blue) and due to changes in deviations of the MOC depth from isopycnals (red). See section 4 for definitions of δD, δD^{isop}, and δD^{diap}. In order to avoid the influence of grid-level noise, the smoothed MOC streamfunction shown in Figure 1 is used here. An equivalent figure that instead uses the raw unsmoothed MOC streamfunction is included in the supporting information (Figure S10). PI = preindustrial; LGM = Last Glacial Maximum.

The MOC streamfunction at the northern edge of the Southern Ocean (30°S; black lines in Figures 2a–2c) can be expressed as

$$\psi(30°\mathrm{S}, \sigma_2) = \phi^{\mathrm{isop}}(\sigma_2) + \phi^{\mathrm{diap}}(\sigma_2), \tag{3}$$

where $\phi^{\mathrm{isop}}(\sigma_2) = \psi(y, \sigma_2)\,|_{\hat{z}(y,\sigma_2)=z_{\mathrm{ref}}}$ denotes the value of the MOC streamfunction at a reference depth z_{ref}. By default we take $z_{\mathrm{ref}} = -1.5$ km to be just below the MML (purple dotted lines in Figure 1). Hence, $\phi^{\mathrm{isop}}(\sigma_2)$ represents the MOC stream function that would occur at 30°S if the circulation were purely adiabatic below z_{ref} (blue lines in Figures 2a–2c). We define $\phi^{\mathrm{diap}}(\sigma_2)$ as the difference between $\psi(30°\mathrm{S}, \sigma_2)$ and $\phi^{\mathrm{isop}}(\sigma_2)$ (red lines in Figures 2a–2c), and hence, it represents the MOC streamfunction component associated with diapycnal mixing below z_{ref} in the Southern Ocean. The MOC depth at 30°S (black squares in Figures 2a–2c) is

$$\mathcal{D} \equiv \hat{z}(30°\mathrm{S}, \sigma_2^*), \tag{4}$$

where σ_2^* is defined to satisfy $\psi(30°\mathrm{S}, \sigma_2^*) = 0$.

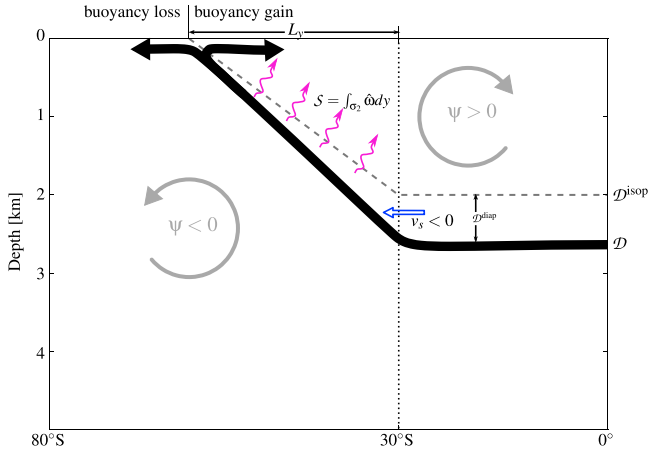

Figure 3. Schematic of the conceptual model used to derive the scaling relationships for the Southern Ocean Meridional Overturning Circulation. The streamline that separates the upper and lower overturning circulation cells ($\hat{\psi} = 0$) is indicated by a thick black line, with arrows indicating the flow direction near the surface. The gray dashed line indicates the isopycnal that connects $z = 0$ at the latitude where buoyancy forcing changes sign. The diapycnal velocity ($\hat{\omega}$) is indicated by purple arrows, and the isopycnal flow (v_s) at the northern edge of the Southern Ocean is represented by a blue arrow. The directions of the overturning circulation in each cell are indicated by gray circle arrows. Volume conservation implies that $-v_s \mathcal{D}^{diap} = \mathcal{S}$, where $\mathcal{S}$ is the latitudinal integration across the Southern Ocean of $\hat{\omega}$ along the isopycnal contour associated with $\mathcal{D}^{isop}$ (gray dashed line). Depth in this schematic is referenced such that the top of the figure ($z = 0$ km) is at the base of the maximum range of the surface mixed layer, rather than the sea surface. This is to exclude the effects of temporal and zonal variations in the isopycnal depth and diapycnal mixing due to mixed layer eddies (see section 3.1).

If the circulation is purely adiabatic, as in Ferrari et al. (2014), the MOC depth can be predicted using the depth of the isopycnal that intersects the streamline $\hat{\psi} = 0$ at the base of the surface mixed layer (blue squares in Figures 2a–2c):

$$\mathcal{D} = \mathcal{D}^{isop} \equiv \hat{z}(30°S, \sigma_2^{**}), \tag{5}$$

where σ_2^{**} is defined to satisfy $\phi^{isop}(\sigma_2^{**}) = 0$. This is indicated by the gray dashed line in Figure 3, and it is constrained by the slope of this isopycnal contour, as well as surface buoyancy forcing and mixed layer processes in the Southern Ocean.

However, due to diapycnal mixing, the simulated MOC depth is deeper than $\mathcal{D}^{isop}$ (see Figure 3). In analogy with equation (3), this can be written as

$$\mathcal{D} = \mathcal{D}^{isop} + \mathcal{D}^{diap}, \tag{6}$$

where $\mathcal{D}^{diap}$ is defined here as the contribution to the MOC depth due to the presence of diapycnal mixing. As can be seen from Figure 3, volume conservation requires that

$$\mathcal{D}^{diap} = -\mathcal{S}/v_s, \tag{7}$$

where $\mathcal{S}$ is the diapycnal velocity $\hat{\omega}$ integrated latitudinally along the isopycnal contour in the Southern Ocean (the gray dashed line south of 30°S in Figure 3) and v_s denotes the residual mean meridional velocity at the northern edge of the Southern Ocean. Note that $v_s < 0$ near the streamline $\hat{\psi} = 0$, so equation (7) implies a positive value of $\mathcal{D}^{diap}$. This relationship (7) arises because there can be no residual flow across the $\hat{\psi} = 0$ streamline.

Equations (6) and (7) show that the MOC depth can be modified below the surface mixed layer by changes in the isopycnal slope ($\mathcal{D}^{isop}$), the intensity of diapycnal mixing ($\mathcal{S}$), and the strength of meridional flow in the Southern Ocean (v_s). This implies that surface forcing in the Northern Hemisphere (such as in the North Atlantic) can affect the MOC depth through its influence on the interhemispheric AMOC strength (v_s) (e.g., Nikurashin & Vallis, 2012), but only if diapycnal mixing in the Southern Ocean is nonnegligible ($\mathcal{S} \neq 0$).

Thus, differences in the MOC depth between any two simulations ($\delta\mathcal{D}$) can be attributed to changes in $\mathcal{D}^{isop}$ and $\mathcal{D}^{diap}$:

$$\delta\mathcal{D} = \delta\mathcal{D}^{isop} + \delta\mathcal{D}^{diap}, \tag{8}$$

where δ denotes the difference in the value of a variable between the two simulations, and

$$\delta\mathcal{D}^{diap} \approx \overline{\mathcal{D}^{diap}} \left(\frac{\delta\mathcal{S}}{\overline{\mathcal{S}}} - \frac{\delta v_s}{\overline{v_s}} \right), \tag{9}$$

where the overline denotes the average between the two simulations being compared and the approximate equality becomes exact in the limit of small differences δv_s and $\delta\mathcal{S}$.

We consider the contributions of $\delta\mathcal{D}^{isop}$ and $\delta\mathcal{D}^{diap}$ to changes in the MOC depth in Figure 2d following equation (8). We find that changes in $\mathcal{D}^{diap}$ between the three simulations are larger than $\mathcal{D}^{isop}$, implying that diapycnal mixing plays a dominant role in changing the MOC depth. This result is largely insensitive to the choice of z_{ref} (Figure S11). A decomposition of $\delta\mathcal{D}^{diap}$ into $\delta\mathcal{S}$ and δv, following equation (9), reveals that changes in $\mathcal{D}^{diap}$ are mostly due to changes in the diapycnal flow $\delta\mathcal{S}$ (Figure S14). Therefore, we conclude that the MOC depth changes in these simulations arise primarily due to differences in diapycnal flow ($\delta\mathcal{S}$), with somewhat smaller but still substantial contributions from changes in the buoyancy forcing integrated through the surface mixed layer and isopycnal slope ($\mathcal{D}^{isop}$). A minor contribution (less than 10% of the total MOC depth changes) comes from changes in isopycnal upwelling (δv_s). The diapycnal transport may be approximated in terms of the simulated diapycnal diffusivity and stratification (cf. Munk, 1966). We find that differences in the diapycnal diffusivity profiles between the three simulations (Figure S12), which occur due

to differences in the density stratification between the three simulations, are consistent with the diapycnal transport differences (Text S3 in the supporting information).

The diapycnal diffusivity profiles in the Southern Ocean that are computed by the model (Figure S12) are within the range of observational estimates from Waterhouse et al. (2014, their Figure 7) and Watson et al. (2013). This suggests that effects of diapycnal mixing on the MOC depth similar to what we find in these simulations may plausibly be expected in nature. Previous studies have suggested that numerical discretization of the nonlinear advection terms in tracer equations can cause substantial numerical diapycnal mixing (e.g., Griffies et al., 2000; Hill et al., 2012), but we find that numerical mixing does not appear to contribute substantially to the diapycnal mixing in these simulations (see Text S3 and Figure S13 in the supporting information).

5. Summary and Discussion

Paleoclimate proxy data suggest that the AMOC was shallower by approximately 1,000 m at the LGM than during the PI period (e.g., Burke et al., 2015; Lund et al., 2011). Previous studies have suggested that this shoaling is dynamically linked to the expansion of the region of negative surface buoyancy forcing in the Southern Ocean (Burke et al., 2015; Ferrari et al., 2014; Watson et al., 2015). In this study, we analyze three ocean-only CESM simulations to investigate the influence of Southern Ocean surface forcing on the depth of the AMOC. In contrast to expectations based on these previous studies (Burke et al., 2015; Ferrari et al., 2014; Watson et al., 2015), we find that applying LGM surface forcing in the Southern Ocean and PI forcing elsewhere causes the AMOC to shoal only about half as much as when LGM surface forcing is applied globally.

We explain the AMOC depth changes through variations in the MOC depth at the northern edge of the Southern Ocean. We develop a scaling relationship that determines this depth as a function of Southern Ocean buoyancy forcing, diapycnal mixing, and isopycnal upwelling. We use this scaling relationship to show that the AMOC depth changes in the CESM simulations arise primarily due to changes in diapycnal transport and isopycnal slope in the Southern Ocean, with a minor contribution from changes in isopycnal upwelling. Therefore, the AMOC depth can be influenced by any processes that affect the buoyancy budget in the surface mixed layer, the isopycnal slope, diapycnal mixing rates, and isopycnal upwelling in the Southern Ocean. These processes, in addition to buoyancy forcing in the Southern Ocean, include the wind stress forcing in the Southern Ocean and surface forcing in the North Atlantic (e.g., Muglia & Schmittner, 2015). The buoyancy loss in the Southern Ocean could also affect the AMOC depth by changing the stratification and hence modifying the diapycnal mixing rate in the Southern Ocean (cf. Jansen & Nadeau, 2016; Marzocchi & Jansen, 2017).

The influence of diapycnal mixing on the AMOC depth is shown schematically in Figure 4. The isopycnal contour that outcrops in the Southern Ocean where the surface buoyancy forcing changes sign (gray dashed line in each panel) also outcrops in the North Atlantic, which occurs due to issues associated with multiple ocean basins that have different density structures (not shown in this single-basin view). Hence, North Atlantic surface forcing can influence the stratification around this isopycnal contour in the Southern Ocean (cf. Nikurashin & Vallis, 2012; Sun et al., 2016). Note that changes in the isopycnal upwelling in the Southern Ocean, which we find to cause less than 10% of the MOC depth difference between the LGM and Test simulations (see section 4), can also be affected by North Atlantic surface forcing changes (e.g., Sun & Liu, 2017; Wolfe & Cessi, 2011). In the case with no diapycnal mixing in the Southern Ocean (left column of Figure 4), the $\hat{\psi} = 0$ streamline (blue cells) follows exactly along the isopycnal contour in the Southern Ocean, so the MOC depth at 30°S is influenced only by the location where the surface buoyancy forcing changes sign as well as the slope of the isopycnal contour, and the stratification does not play a role. In the diabatic case (right column in Figure 4), by contrast, the stratification can influence the level of diapcynal mixing close to the $\hat{\psi} = 0$ streamline, and hence, changes in North Atlantic surface forcing can modify the MOC depth at 30°S. Using an idealized setup that has only one basin, Jansen (2017) shows that the Northern Hemisphere surface forcing has a modest effect on the AMOC depth and contributes only ∼15% of the AMOC depth shoaling in his simulations of the LGM (compare "LGM dTSH" and "LGM" with "PI" in his Table 1). This suggests that the influence of North Atlantic surface forcing on the AMOC depth changes may depend on the complexity of the model.

There are some caveats associated with the model used in this study. The nominal 1° ocean resolution in CESM does not resolve eddies, which have been shown to be important in the response of the Southern Ocean circulation to perturbations in the surface forcing (e.g., Abernathey et al., 2011; Munday et al., 2013), nor does it resolve the near coastal processes in the Antarctic regions, which have been suggested to be important for the

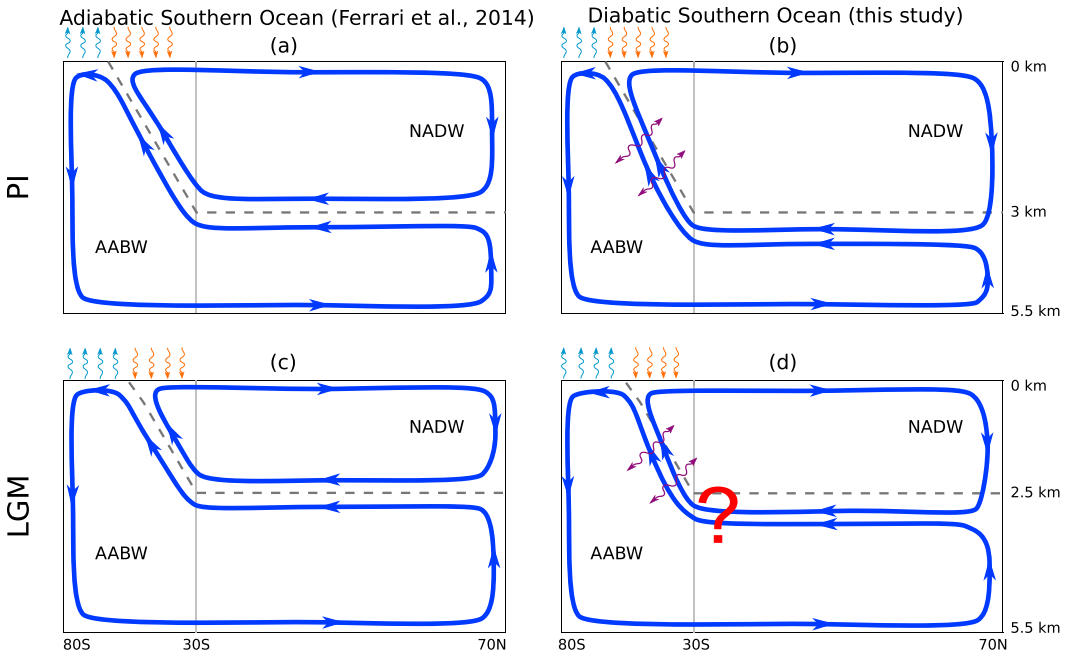

Figure 4. Schematic diagrams illustrating theories for how Southern Ocean buoyancy forcing influences the global ocean circulation. (a, b) Preindustrial (PI) ocean. (c, d) Last Glacial Maximum (LGM) ocean. Panels on the left side (a and c) represent the theory that the circulation is adiabatic in the Southern Ocean (Ferrari et al., 2014). In this case, the Atlantic Meridional Overturning Circulation (AMOC) depth can be predicted from the Southern Ocean surface buoyancy forcing (arrows above the Southern Ocean surface; upward for buoyancy loss and downward for buoyancy gain). Panels on the right side (b and d) correspond to the case of a circulation that is more diabatic in the Southern Ocean, as suggested by our findings as well as in situ measurements (e.g., Whalen et al., 2012). In this case, the AMOC depth is sensitive to the amount of diapycnal mixing in the Southern Ocean (purple double arrows), which is influenced by the surface forcing outside the Southern Ocean through its effect on the Southern Ocean density stratification. Hence, the AMOC depth cannot be predicted from the Southern Ocean surface buoyancy forcing alone; this is indicated as a red question mark in panel (d). The gray dashed line in each panel represents the isopycnal that outcrops in the Southern Ocean at the latitude where surface buoyancy flux changes sign. This schematic represents an idealized two-dimensional view of the overturning circulation; the rearrangement of the three-dimensional overturning circulation associated with the AMOC shoaling may also play an important role (cf. Ferrari et al., 2014). As in Figure 3, the depth is referenced here to the base of the surface mixed layer. NADW = North Atlantic Deep Water; AABW = Antarctic Bottom Water.

simulation of AABW production (e.g., Newsom et al., 2016; Snow et al., 2016). Nonetheless, the present study highlights the importance of diapycnal mixing in the Southern Ocean, which has typically been neglected in previous conceptual model studies of the deep ocean stratification (e.g., Nikurashin & Vallis, 2011; Stewart et al., 2014; Sun et al., 2016). Diapycnal mixing in the Southern Ocean can be neglected in these studies as long as the diapycnal transport below the surface mixed layer in the Southern Ocean is small compared to the ocean basins to the north, such that the buoyancy budget is predominantly balanced between the Southern Ocean surface buoyancy forcing and diapycnal mixing in the basins north of the Southern Ocean. This appears to apply for the world oceans mainly because the Southern Ocean is much smaller than the total area of the basins north of it. However, the results of the present study suggest that diapycnal mixing in the Southern Ocean must be considered in order to describe the influence of Southern Ocean surface forcing on the depth of the AMOC.

A number of factors further complicate the adiabatic picture presented in Ferrari et al. (2014). First, Schmittner et al. (2015) suggest that the global mean diapycnal diffusivity was larger at the LGM by a factor of 3 compared to the present ocean as a result of the lower sea level, which shifts tidal mixing from shallow coastal regions into the deep ocean. This implies a possibly even larger influence of diapycnal mixing on the AMOC depth at the LGM than was found here. Second, Muglia and Schmittner (2015) find that a number of other current climate models simulate a deeper AMOC under LGM forcing, in contrast to CCSM4. These models have expanded Southern Ocean sea ice cover in their LGM simulations (Marzocchi & Jansen, 2017, their Figure 3) but nonetheless do not simulate a shoaling of the AMOC, implying that the connection between Southern Ocean surface forcing and AMOC depth may not be a robust result among current climate models. Third, the

buoyancy forcing tends to be weak in the vicinity of the latitude of zero-buoyancy forcing (Figure S2). Therefore, the overturning circulation close to the zero-buoyancy flux region could be overwhelmed by processes in the surface mixed layer (cf. Karsten et al., 2002; Marshall et al., 1999) or by standing eddies associated with the complex three-dimensional structure of the Southern Ocean circulation (Tréguier et al., 2007), further weakening the link between Southern Ocean surface buoyancy forcing and the AMOC depth and highlighting the role of other processes within and outside the Southern Ocean.

In summary, this study used CESM ocean-only simulations to investigate the influence of Southern Ocean surface forcing on the AMOC depth, which is believed to play an important role in glacial-interglacial changes in atmospheric CO_2. The results suggest that the AMOC depth is sensitive to both Southern Ocean and North Atlantic surface buoyancy forcing due to diapcynal mixing in the Southern Ocean.

Acknowledgments
Without implying their endorsement, we thank Paola Cessi, Shang-Ping Xie, Lynne Talley, Raffaele Ferrari, Malte Jansen, Jess Adkins, and Paul Kushner for helpful comments and discussions. This work was supported by the National Science Foundation (NSF) [10.13039/100000001] (OCE-1357078, PLR-1543338, and OPP-1643445). Files related to the setup of the CESM simulations, as well as processed model output, are available at http://eisenman.ucsd.edu/code.html. Unprocessed model output is available by request from the corresponding author.

References

Abernathey, R., Marshall, J., & Ferreira, D. (2011). The dependence of Southern Ocean meridional overturning on wind stress. *Journal of Physical Oceanography*, *41*(12), 2261–2278.
Ballarotta, M., Drijfhout, S., Kuhlbrodt, T., & Döös, K. (2013). The residual circulation of the Southern Ocean: Which spatio-temporal scales are needed?. *Ocean Modelling*, *64*, 46–55.
Bishop, S. P., Gent, P. R., Bryan, F. O., Thompson, A. F., Long, M. C., & Abernathey, R. (2016). Southern Ocean overturning compensation in an eddy-resolving climate simulation. *Journal of Physical Oceanography*, *46*(5), 1575–1592.
Böning, C. W., Dispert, A., Visbeck, M., Rintoul, S., & Schwarzkopf, F. U. (2008). The response of the Antarctic Circumpolar Current to recent climate change. *Nature Geoscience*, *1*(12), 864–869.
Brady, E. C., Otto-Bliesner, B. L., Kay, J. E., & Rosenbloom, N. (2013). Sensitivity to glacial forcing in the CCSM4. *Journal of Climate*, *26*(6), 1901–1925.
Brovkin, V., Ganopolski, A., Archer, D., & Rahmstorf, S. (2007). Lowering of glacial atmospheric CO_2 in response to changes in oceanic circulation and marine biogeochemistry. *Paleoceanography*, *22*, PA4202. https://doi.org/10.1029/2006PA001380
Burke, A., Stewart, A. L., Adkins, J. F., Ferrari, R., Jansen, M. F., & Thompson, A. F. (2015). The glacial mid-depth radiocarbon bulge and its implications for the overturning circulation. *Paleoceanography*, *30*, 1021–1039. https://doi.org/10.1002/2015PA002778
Danabasoglu, G., Bates, S. C., Briegleb, B. P., Jayne, S. R., Jochum, M., Large, W. G., et al. (2012). The CCSM4 ocean component. *Journal of Climate*, *25*(5), 1361–1389.
Ferrari, R., Jansen, M. F., Adkins, J. F., Burke, A., Stewart, A. L., & Thompson, A. F. (2014). Antarctic sea ice control on ocean circulation in present and glacial climates. *Proceedings of the National Academy of Sciences of the United States of America*, *111*(24), 8753–8758.
Gent, P. R., & Danabasoglu, G. (2011). Response to increasing Southern Hemisphere winds in CCSM4. *Journal of Climate*, *24*(19), 4992–4998.
Gent, P. R., & Mcwilliams, J. C. (1990). Isopycnal mixing in ocean circulation models. *Journal of Physical Oceanography*, *20*(1), 150–155.
Gent, P. R., Danabasoglu, G., Donner, L. J., Holland, M. M., Hunke, E. C., Jayne, S. R., et al. (2011). The community climate system model version 4. *Journal of Climate*, *24*(19), 4973–4991.
Gersonde, R., Abelmann, A., Brathauer, U., Becquey, S., Bianchi, C., Cortese, G., et al. (2003). Last glacial sea surface temperatures and sea-ice extent in the Southern Ocean (Atlantic-Indian sector): A multiproxy approach. *Paleoceanography*, *18*(3), 1061. https://doi.org/10.1029/2002PA000809
Gersonde, R., Crosta, X., Abelmann, A., & Armand, L. (2005). Sea-surface temperature and sea ice distribution of the Southern Ocean at the EPILOG Last Glacial Maximum—A circum-Antarctic view based on siliceous microfossil records. *Quaternary Science Reviews*, *24*(7), 869–896.
Griffies, S. M., Pacanowski, R. C., & Hallberg, R. W. (2000). Spurious diapycnal mixing associated with advection in a *z*-coordinate ocean model. *Monthly Weather Review*, *128*(3), 538–564.
Hill, C., Ferreira, D., Campin, J.-M., Marshall, J., Abernathey, R., & Barrier, N. (2012). Controlling spurious diapycnal mixing in eddy-resolving height-coordinate ocean models—Insights from virtual deliberate tracer release experiments. *Ocean Modelling*, *45*, 14–26.
Iudicone, D., Madec, G., Blanke, B., & Speich, S. (2008). The role of Southern Ocean surface forcings and mixing in the global conveyor. *Journal of Physical Oceanography*, *38*(7), 1377–1400.
Jackett, D. R., & McDougall, T. J. (1997). A neutral density variable for the world's oceans. *Journal of Physical Oceanography*, *27*(2), 237–263.
Jansen, M. F. (2017). Glacial ocean circulation and stratification explained by reduced atmospheric temperature. *Proceedings of the National Academy of Sciences of the United States of America*, *114*(1), 45–50.
Jansen, M. F., & Nadeau, L.-P. (2016). The effect of southern ocean surface buoyancy loss on the deep ocean circulation and stratification. *Journal of Physical Oceanography*, *46*(11), 3455–3470. https://doi.org/10.1175/JPO-D-16-0084.1
Jayne, S. R. (2009). The impact of abyssal mixing parameterizations in an ocean general circulation model. *Journal of Physical Oceanography*, *39*(7), 1756–1775.
Karsten, R., Jones, H., & Marshall, J. (2002). The role of eddy transfer in setting the stratification and transport of a circumpolar current. *Journal of Physical Oceanography*, *32*(1), 39–54.
Large, W. G., Danabasoglu, G., Doney, S. C., & McWilliams, J. C. (1997). Sensitivity to surface forcing and boundary layer mixing in a global ocean model: Annual-mean climatology. *Journal of Physical Oceanography*, *27*(11), 2418–2447.
Large, W. G., McWilliams, J. C., & Doney, S. C. (1994). Oceanic vertical mixing: A review and a model with a nonlocal boundary layer parameterization. *Reviews of Geophysics*, *32*(4), 363–403.
Lozier, M. S. (2012). Overturning in the North Atlantic. *Annual Review of Marine Science*, *4*, 291–315.
Lund, D., Adkins, J., & Ferrari, R. (2011). Abyssal Atlantic circulation during the Last Glacial Maximum: Constraining the ratio between transport and vertical mixing. *Paleoceanography*, *26*, PA1213. https://doi.org/10.1029/2010PA001938
Marshall, J., Jamous, D., & Nilsson, J. (1999). Reconciling thermodynamic and dynamic methods of computation of water-mass transformation rates. *Deep-Sea Research Part I*, *46*(4), 545–572.
Marzocchi, A., & Jansen, M. F. (2017). Connecting Antarctic sea ice to deep-ocean circulation in modern and glacial climate simulations. *Geophysical Research Letters*, *44*, 6286–6295. https://doi.org/10.1002/2017GL073936
Mashayek, A., Ferrari, R., Merrifield, S., Ledwell, J. R., St Laurent, L., & Naveira Garabato, A. (2017). Topographic enhancement of vertical turbulent mixing in the Southern Ocean. *Nature Communications*, *8*, 14197.

Mazloff, M. R., Ferrari, R., & Schneider, T. (2013). The force balance of the Southern Ocean meridional overturning circulation. *Journal of Physical Oceanography*, *43*(6), 1193–1208.
Mazloff, M. R., Heimbach, P., & Wunsch, C. (2010). An eddy-permitting Southern Ocean state estimate. *Journal of Physical Oceanography*, *40*(5), 880–899.
McDougall, T. J. (1987). Neutral surfaces in the ocean: Implications for modelling. *Geophysical Research Letters*, *14*(8), 797–800.
Monnin, E., Indermühle, A., Dällenbach, A., Flückiger, J., Stauffer, B., Stocker, T. F., et al. (2001). Atmospheric CO_2 concentrations over the last glacial termination. *Science*, *291*(5501), 112–114.
Muglia, J., & Schmittner, A. (2015). Glacial Atlantic overturning increased by wind stress in climate models. *Geophysical Research Letters*, *42*, 9862–9868. https://doi.org/10.1002/2015GL064583
Munday, D. R., Johnson, H. L., & Marshall, D. P. (2013). Eddy saturation of equilibrated circumpolar currents. *Journal of Physical Oceanography*, *43*(3), 507–532.
Munk, W. H. (1966). Abyssal recipes. *Deep-Sea Research*, *13*, 707–730.
Naveira Garabato, A. C., Polzin, K. L., King, B. A., Heywood, K. J., & Visbeck, M. (2004). Widespread intense turbulent mixing in the Southern Ocean. *Science*, *303*(5655), 210–213.
Newsom, E. R., Bitz, C. M., Bryan, F. O., Abernathey, R., & Gent, P. R. (2016). Southern Ocean deep circulation and heat uptake in a high-resolution climate model. *Journal of Climate*, *29*(7), 2597–2619.
Nikurashin, M., & Vallis, G. (2011). A theory of deep stratification and overturning circulation in the ocean. *Journal of Physical Oceanography*, *41*(3), 485–502.
Nikurashin, M., & Vallis, G. (2012). A theory of the interhemispheric meridional overturning circulation and associated stratification. *Journal of Physical Oceanography*, *42*(10), 1652–1667.
Nurser, A. G., & Lee, M.-M. (2004). Isopycnal averaging at constant height. Part I: The formulation and a case study. *Journal of Physical Oceanography*, *34*(12), 2721–2739.
Otto-Bliesner, B., Hewitt, C., Marchitto, T., Brady, E., Abe-Ouchi, A., Crucifix, M., et al. (2007). Last Glacial Maximum ocean thermohaline circulation: PMIP2 model intercomparisons and data constraints. *Geophysical Research Letters*, *34*, L12706. https://doi.org/10.1029/2007GL029475
Otto-Bliesner, B. L., Brady, E. C., Clauzet, G., Tomas, R., Levis, S., & Kothavala, Z. (2006). Last Glacial Maximum and Holocene climate in CCSM3. *Journal of Climate*, *19*(11), 2526–2544.
Sarmiento, J. L., & Gruber, N. (2002). Sinks for anthropogenic carbon. *Physics Today*, *August*, 30–36.
Schmittner, A., Green, J., & Wilmes, S.-B. (2015). Glacial ocean overturning intensified by tidal mixing in a global circulation model. *Geophysical Research Letters*, *42*, 4014–4022. https://doi.org/10.1002/2015GL063561
Sigman, D. M., Hain, M. P., & Haug, G. H. (2010). The polar ocean and glacial cycles in atmospheric CO_2 concentration. *Nature*, *466*(7302), 47–55.
Snow, K., Hogg, A. M., Sloyan, B. M., & Downes, S. M. (2016). Sensitivity of Antarctic bottom water to changes in surface buoyancy fluxes. *Journal of Climate*, *29*(1), 313–330.
Stewart, A. L., Ferrari, R., & Thompson, A. F. (2014). On the importance of surface forcing in conceptual models of the deep ocean. *Journal of Physical Oceanography*, *44*(3), 891–899.
Sun, S., & Liu, J. (2017). Sensitivity of the Antarctic Circumpolar Current transport to surface buoyancy conditions in the North Atlantic. *Ocean Modelling*, *118*, 118–129.
Sun, S., Eisenman, I., & Stewart, A. L. (2016). The influence of southern ocean surface buoyancy forcing on glacial-interglacial changes in the global deep ocean stratification. *Geophysical Research Letters*, *43*, 8124–8132. https://doi.org/10.1002/2016GL070058
Talley, L. D. (2013). Closure of the global overturning circulation through the Indian, Pacific, and Southern Oceans: Schematics and transports. *Oceanography*, *26*(1), 80–97.
Tréguier, A.-M., England, M., Rintoul, S., Madec, G., Le Sommer, J., & Molines, J.-M. (2007). Southern Ocean overturning across streamlines in an eddying simulation of the Antarctic Circumpolar Current. *Ocean Science*, *4*(4), 653–698.
Viebahn, J., & Eden, C. (2010). Towards the impact of eddies on the response of the Southern Ocean to climate change. *Ocean Modelling*, *34*(3), 150–165.
Walin, G. (1982). On the relation between sea-surface heat flow and thermal circulation in the ocean. *Tellus*, *34*(2), 187–195.
Waterhouse, A. F., MacKinnon, J. A., Nash, J. D., Alford, M. H., Kunze, E., Simmons, H. L., et al. (2014). Global patterns of diapycnal mixing from measurements of the turbulent dissipation rate. *Journal of Physical Oceanography*, *44*(7), 1854–1872.
Watson, A. J., Ledwell, J. R., Messias, M.-J., King, B. A., Mackay, N., Meredith, M. P., et al. (2013). Rapid cross-density ocean mixing at mid-depths in the Drake Passage measured by tracer release. *Nature*, *501*(7467), 408.
Watson, A. J., Vallis, G. K., & Nikurashin, M. (2015). Southern Ocean buoyancy forcing of ocean ventilation and glacial atmospheric CO_2. *Nature Geoscience*, *8*(11), 861–864.
Whalen, C., Talley, L., & MacKinnon, J. (2012). Spatial and temporal variability of global ocean mixing inferred from Argo profiles. *Geophysical Research Letters*, *39*, L18612. https://doi.org/10.1029/2012GL053196
Wolfe, C. L., & Cessi, P. (2010). What sets the strength of the middepth stratification and overturning circulation in eddying ocean models? *Journal of Physical Oceanography*, *40*(7), 1520–1538.
Wolfe, C. L., & Cessi, P. (2011). The adiabatic pole-to-pole overturning circulation. *Journal of Physical Oceanography*, *41*(9), 1795–1810.
Wu, L., Jing, Z., Riser, S., & Visbeck, M. (2011). Seasonal and spatial variations of Southern Ocean diapycnal mixing from Argo profiling floats. *Nature Geoscience*, *4*(6), 363–366.
Zhang, X., Lohmann, G., Knorr, G., & Xu, X. (2013). Different ocean states and transient characteristics in Last Glacial Maximum simulations and implications for deglaciation. *Climate of the Past*, *9*(5), 2319.

Supporting Information for "Does Southern Ocean surface forcing shape the global ocean overturning circulation?"

Shantong Sun,[1] Ian Eisenman,[1] and Andrew L. Stewart [2]

[1] Scripps Institution of Oceanography, University of California, San Diego, La Jolla, USA
[2] Department of Atmospheric and Oceanic Sciences, University of California, Los Angeles, USA

Contents of this file

1. Text S1 to S3
2. Figures S1 to S13

Introduction

This Supporting Information comprises three sections of text and fourteen figures. In Text S1, the CESM simulation set-up is described in detail. In Text S2, we evaluate the changes in isopycnal slope. In Text S3, we present further discussions on the diapycnal mixing in our model.

Text S1. CESM setup

The ocean component of CESM is the Parallel Ocean Program version 2 (POP2), of which the horizontal resolution is nominally 1° with the north pole of the ocean grid displaced to Greenland. It has 60 vertical levels with thicknesses that range from 10 m at the sea surface to 250 m at the ocean bottom. The coupled CCSM4 simulations of the PI simulations [*Gent et al.*, 2011] and the coupled LGM simulations [*Brady et al.*, 2013], from which the forcing in this study is derived, share the same ocean grid configuration. The coupled simulations have a resolution of $1.9° \times 2.5°$ for the land and atmosphere, and it has the same resolution for sea ice component as for the ocean. The unresolved mesoscale eddies are parameterized using the Gent-McWilliams scheme [*Gent and Mcwilliams*, 1990] with a thickness diffusivity that varies proportionally to the local density stratificiation [*Gent and Danabasoglu*, 2011]. The vertical convection is handled by the non-local K-Profile Parameterization (KPP) scheme [*Large et al.*, 1994].

For atmospheric forcing, including precipitation, solar radiation, surface winds speed, atmospheric pressure, and atmospheric humidity, we use output that is reported by the CCSM4 coupler every 3 hours. The atmosphere-ocean fluxes, including evaporation, wind stress, upward longwave radiation, latent heat flux, and sensible heat flux, are calculated in the ocean-only runs based on the simulated ocean state and the specified atmospheric state. For ice-related forcing, including sea ice concentration and heat flux between the ice and ocean, we use daily-mean data reported by the CCSM sea ice component (CICE). For other ice-related forcing, river runoff, and glacial runoff, we use monthly-mean data. In each case, the coupled model output is used to construct surface forcing fields that repeat every 30 years. The first 10 years of the last 30-year forcing cycle in each run are excluded in our analysis in order to avoid the adjustment associated with the jump in the forcing at the beginning of each 30-year cycle. For further details, the readers are referred to the supporting information in *Sun et al.* [2016].

Corresponding author: Shantong Sun, shantong@ucsd.edu

The time- and zonal-mean wind stress and wind stress curl is presented in Figure S1. Consistent with our model setup, the wind stress forcing in the Test run closely follows the LGM run in the Southern Ocean until 40°S. Unlike the wind stress forcing, surface buoyancy flux in the Test run appears to differ from LGM (Figure S2). This is because more frazil ice is formed in the LGM run due to a colder global ocean temperature, which releases more brine and increases the negative buoyancy loss close to the Antarctica. The frazil ice is formed as part of the ocean model when the temperature of seawater falls below the freezing point.

In Figure S2d, we present the zonal-mean buoyancy flux from the Southern Ocean State Estimate [SOSE; *Mazloff et al.*, 2010], which broadly resembles our PI simulation. However, the latitude where surface buoyancy forcing changes sign in SOSE is further south by 5° latitude compared to our PI simulations. Therefore, this study does not aim to reproduce the ocean circulation in the PI and LGM climate. Instead, we focus on the response of the AMOC depth to changes in the surface buoyancy forcing in the Southern Ocean.

Previous studies suggest that the simulated AMOC could be biased from the equilibrium state due to a lack of equilibration for the deep ocean circulation in climate models [e.g., *Zhang et al.*, 2013; *Marzocchi and Jansen*, 2017]. In order to evaluate the potential influence of model equilibrium on our results, here we use the residual-mean overturning circulation ($\tilde{\psi}$), which is reported by the model and represents the sum of the Eulerian-mean overturning circulation and eddy bolus contributions, instead of the isopycnal overturning circulation (ψ) as in the main article. The residual-mean overturning circulation is a good approximation to the isopycnal overturning circulation in the basin, where the eddy activities are relatively low. We define the AMOC strength as the maximum residual-mean overturning circulation streamfunction below 500m and the AMOC depth as the depth where $\tilde{\psi}(y, z) = 0$ in the Atlantic averaged between 30°S and 0° (Figure S3). Note that the AMOC depth defined using $\tilde{\psi}$ is not qualitatively different from that using $\hat{\psi}$ (compare Figure S3 with Figure 1). Over the last 120 years, the trends in the annual-mean AMOC strength (thin lines in Figure S3) are -0.28 Sv/century, -0.17 Sv/century, and -0.64 Sv/century for the PI, Test, and LGM runs; and the trends in the annual-mean AMOC depth (thin lines in Figure S3) defined using $\tilde{\psi}$ is -0.45 m/year, -0.04 m/year, and -0.24 m/year for the PI, Test, and LGM runs, respectively. This implies that, if these trends persist, the AMOC depth in the Test run would be closer to the PI run and farther from the LGM run following a longer model simulation. Therefore, the lack of equilibrium will not affect our conclusion that the Southern Ocean surface buoyancy forcing alone can not determine the depth of the AMOC in our model.

Text S2. Isopycnal slope

It is hypothesized that the isopycnal slope is constant between the PI and LGM climate in *Ferrari et al.* [2014]. However, small changes in the isopycnal slope in response to surface forcing perturabtions are present in both observations [*Böning et al.*, 2008] and models [e.g., *Viebahn and Eden*, 2010; *Gent and Danabasoglu*, 2011; *Wolfe and Cessi*, 2010] that could potentially cause discernible changes in the MOC depth. Here, we quantify the changes in the isopycnal slope between the three ocean-only simulations. Instead of calculating the isopycnal slope directly, we calculate the depth changes of isopycnals from 60°S to 30°S ($\Delta\hat{z}_1$; Figure S8):

$$\Delta\hat{z} = \hat{z}(60^\circ\mathrm{S}, \sigma_2) - \hat{z}(30^\circ\mathrm{S}, \sigma_2). \tag{S1}$$

They are mapped to depth coordinates using the mean depth of isopycnals at 50°S in Figure S8. Comparison of $\Delta\hat{z}$ between the simulations in Figure S8b reveals that a depth difference of around 50m in the MOC depth between Test and LGM simulations could be purely attributed to the small changes in the isopycnal slope (Figure 2d), although these changes in isopycnal slope are difficult to discern by eyes (Figure S7).

Test S3. Diapycnal mixing

Following the framework of *Walin* [1982], we can calculate the water mass transformation due to surface buoyancy forcing as

$$\mathcal{T}(\sigma_2) = -\frac{1}{T}\frac{\partial}{\partial \sigma_2}\int_0^T \iint_{90^\circ\mathrm{S}<y<30^\circ\mathrm{S}} \mathcal{H}(\sigma_2'(x,y,0,t)-\sigma_2)F_s(x,y,t)dAdt, \tag{S2}$$

where $F_s(x,y,t)$ represents the surface buoyancy flux in the Southern Ocean. If the circulation is purely adiabatic, $\mathcal{T}(\sigma_2)$ (blue lines in Figure S9) should be the same as $\psi(30^\circ\mathrm{S},\sigma_2)$ (black lines in Figure S9). The difference between the two, $\mathcal{T}(\sigma_2)-\psi(30^\circ\mathrm{S},\sigma_2)$, represents the water mass transformation due to diapycnal mixing in the Southern Ocean (red lines in Figure S9). Similar to *Newsom et al.* [2016], we find that the water mass transformation due to diapycnal mixing is substantial in the Southern Ocean in our study. By comparing Figure S9 with Figure 2 in the main article, it appears that most of the diapycnal mixing (~15 Sv out of 20 Sv) observed in Figure S9 occurs in the surface 1500 m in CESM.

In Figure S12, we plot the mean diapycnal diffusivity between 60°S and 30°S with respect to depth (Figure S12a) and height above the ocean bottom (Figure S12b), which is within the observed range of diapycnal diffusivity [*Waterhouse et al.*, 2014, their Fig.7]. We also calculate the mean diapycnal diffusivity close to the domain of the diapycnal and isopycnal mixing experiment in the Southern Ocean (DIMES), denoted by the two rectangulars in Figure S12b. We find a diapycnal diffusivity of $\sim 1.4\times10^{-4}\mathrm{m}^2/\mathrm{s}$ at 1500m depth, which is consistent with *Watson et al.* [2013] that concludes the diapycnal diffusivity to be $O(10^{-4})\mathrm{m}^2/\mathrm{s}$ at the same depth around the same region from tracer distributions in the DIMES project. This suggests that similar effects of diapycnal mixing on the MOC depth, as discussed in the main article, could be plausibly expected in the real ocean.

Unless in regions of deep convection or in the boundary layer, the diapycnal diffusivity profile is dominated by the parameterized tidally-driven mixing, which scales inversely with the density stratification [*Jayne*, 2009]. The diapycnal diffusivity is largest between 1.5km and 3.5km depth in Figure S12a due to its weak stratification [*Sun et al.*, 2016]. This explains the largest contribution of diapycnal mixing to the MOC depth in Figure S11b. The magnitude of the diapycnal diffusivity in the Test run falls between those of the PI run and LGM run, consistent with the diapycnal mixing in Figure S11b. This suggests that the differences in diapycnal mixing can be partly attributed to the intensity of the surface buoyancy forcing in the Southern Ocean [cf. *Sun et al.*, 2016].

Previous studies have suggested that numerical discretization of the nonlinear advection terms in tracer equation can cause substantial numerical diapycnal diffusion [e.g., *Griffies et al.*, 2000; *Hill et al.*, 2012]. Here, we quantify how much of the diapycnal mixing could be associated with discretization errors by defining an effective diapycnal diffusivity. The effective diapycnal diffusivity (κ_{eff}) is defined as:

$$\hat{\omega}\frac{\partial\hat{\sigma}_2}{\partial z} = \frac{\partial}{\partial z}\left(\hat{\kappa}_{\mathrm{eff}}\frac{\partial\hat{\sigma}_2}{\partial z}\right), \tag{S3}$$

following the notation of *Munk* [1966], where the hat "$\hat{}$" denotes quantities in depth coordinates as in the main article and $\hat{\omega}$ represents the diapycnal velocity and $\hat{\omega}(y,\hat{z}(y,\sigma_2)) = \omega(y,\sigma_2) = \frac{1}{L_x}\frac{\partial\psi(y,\sigma_2)}{\partial y}$. A small isopycnal slope has been assumed to derive (S3). For regions below the surface mixed layer and away from deep convection zones, the water column is stably stratified and the effective diapycnal diffusivity can be obtained in σ_2 coordinates as:

$$\kappa_{\mathrm{eff}}(\sigma_2) = \frac{1}{L}\int_0^L \frac{\partial\hat{z}(y,\sigma_2)}{\partial\sigma_2}\left(\int_{\sigma_2^{\max}}^{\sigma_2}\omega(y,\sigma_2')\,d\sigma_2'\right)dy, \tag{S4}$$

where $\kappa_{\mathrm{eff}}(\sigma_2) = \frac{1}{L}\int_0^L \hat{\kappa}_{\mathrm{eff}}(y,\hat{z}(y,\sigma_2))dy$, L is the meridional length of the integration, is the diapycnal velocity in σ_2 coordinates, and $\hat{z}(y,\sigma_2)$ represents the mean depth of isopycnal, as defined in the main article.

For comparison, the parameterized diapycnal diffusivity is also mapped to σ_2 coordinates as

$$\kappa(\sigma_2) = \frac{1}{T}\int_0^T \frac{1}{A}\iint \kappa_m(x, y, z, t)|_{\sigma_2'(x,y,z,t)=\sigma_2}\, dx\, dy\, dt, \tag{S5}$$

where $\kappa_m(x, y, z, t)$ is the model reported diapycnal diffusivity, and A represents the integral area on isopycnals.

We compare the diagnosed effective diapycnal diffusivity κ_{eff} with the model reported diapycnal diffusivity κ in Figure S13. It appears that the effective diapycnal diffusivity is approximately the same as the the model-reported value, implying that the numerical diapycnal mixing is not playing a significant role in CESM. Here, we have limited the calculation of κ_{eff} and κ in the deep ocean and within 30°S and 30°N. This is because a stable stratification is required in Equations (S3) and (S5) and the calculation might be not reliable in the Southern Ocean. Therefore, we cannot exclude the possibility of a larger fraction of the diapycnal mixing being due to numerical discretization errors in the Southern Ocean.

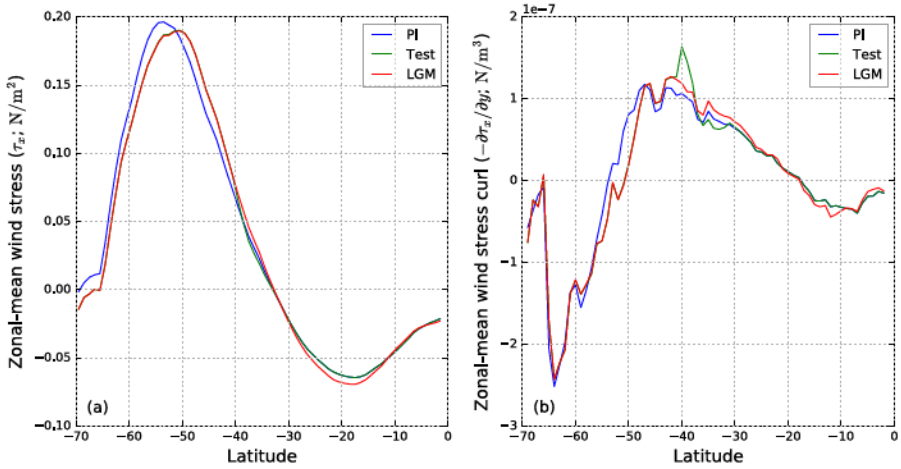

Figure S1. Zonal mean wind stress (a) and wind stress curl (b). Note that the slightly enhanced wind stress curl in the Test simulation close to 40°S is due to the feathering of the forcing fields between 40°S and 30°S.

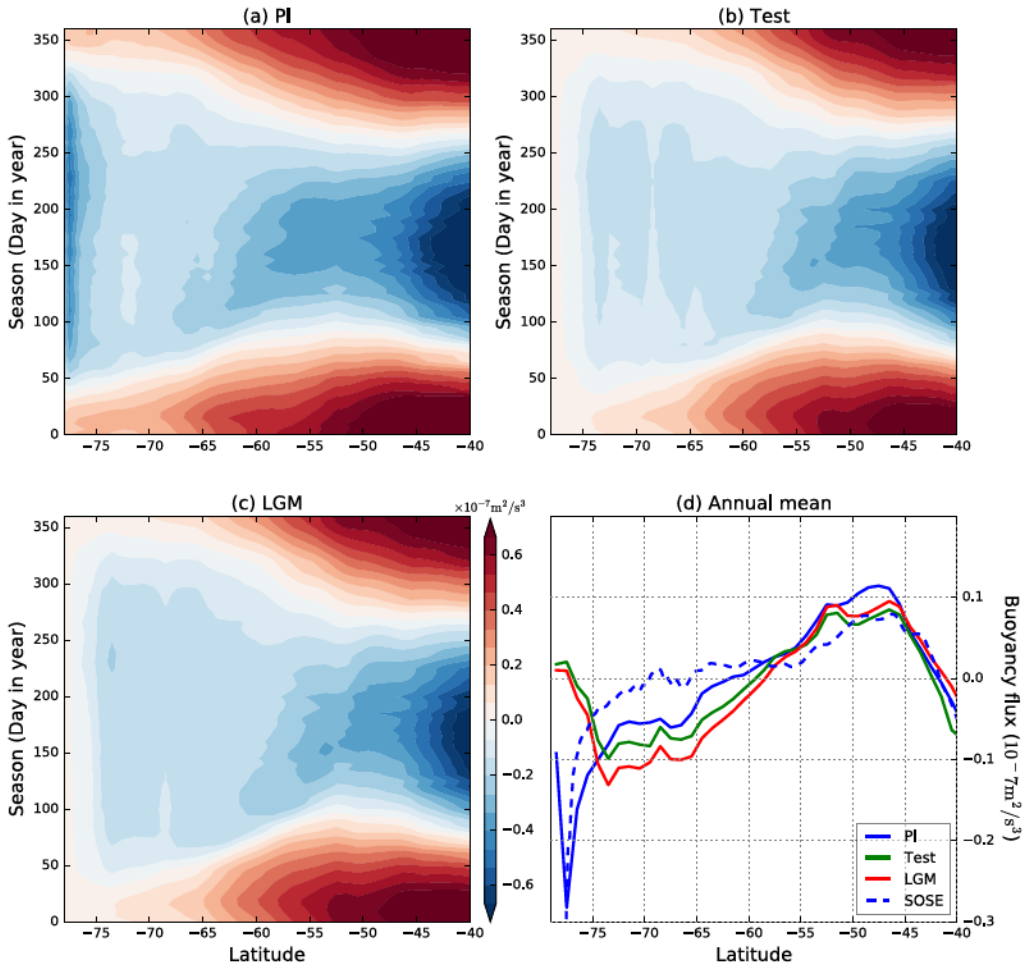

Figure S2. Long-term mean seasonally-varying zonal-mean buoyancy flux (a-c) and annual-mean buoyancy flux (d) from the three ocean-only simulations. The time- and zonal-mean buoayncy flux over years 2005-2010 from the Southern Ocean State Estimate [SOSE; ***Mazloff et al.***, 2010] is plotted in panel d as a blue dashed line for comparison.

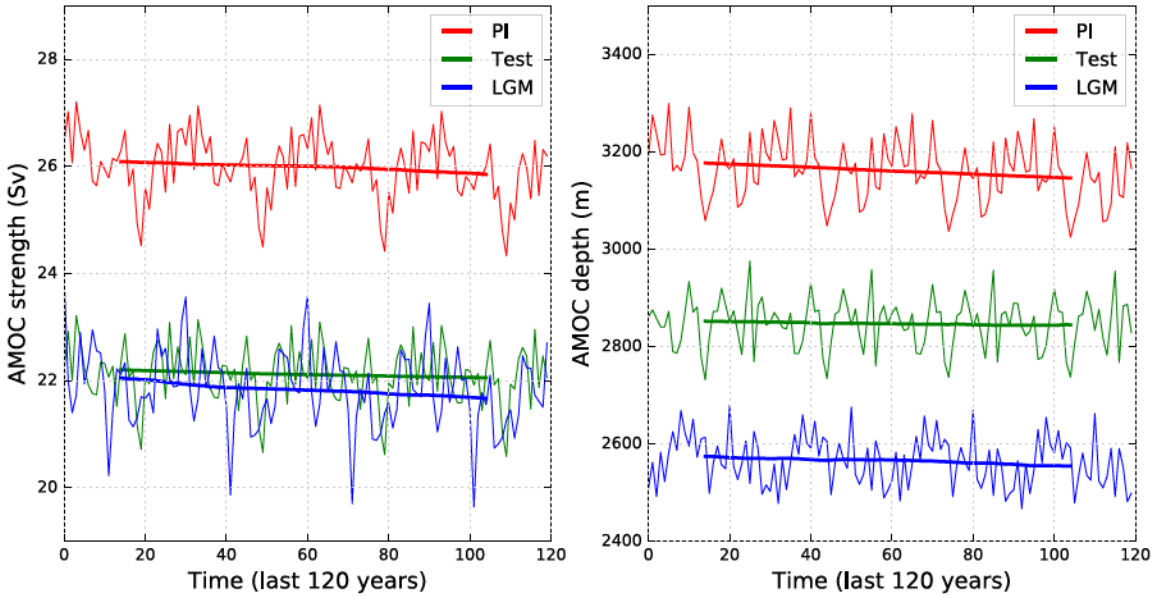

Figure S3. Annual-mean AMOC strength (left) and depth (right) over the last 120 years of the simulations. The thick lines represent 30-year running averages of the annual-mean data. The AMOC depth is averaged between 30°S and 0° in the Atlantic Ocean.

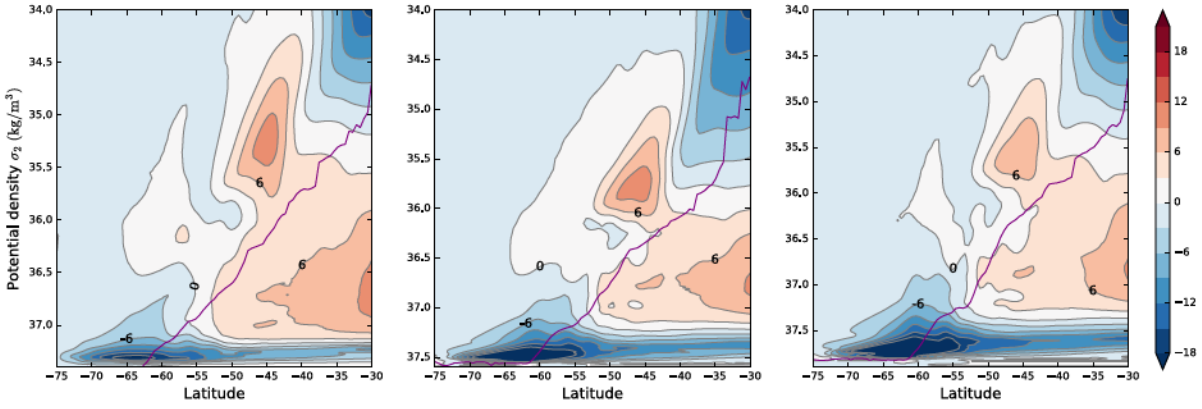

Figure S4. The MOC streamfunction on σ_2 coordinates in the Southern Ocean, with the contours and colorbar labeled in units of Sv. The purple line represents the maximum potential density that appears in the surface mixed layer at each latitude for any time and any longitude. Therefore, isopycnals below the purple line always lie below the surface mixed layer.

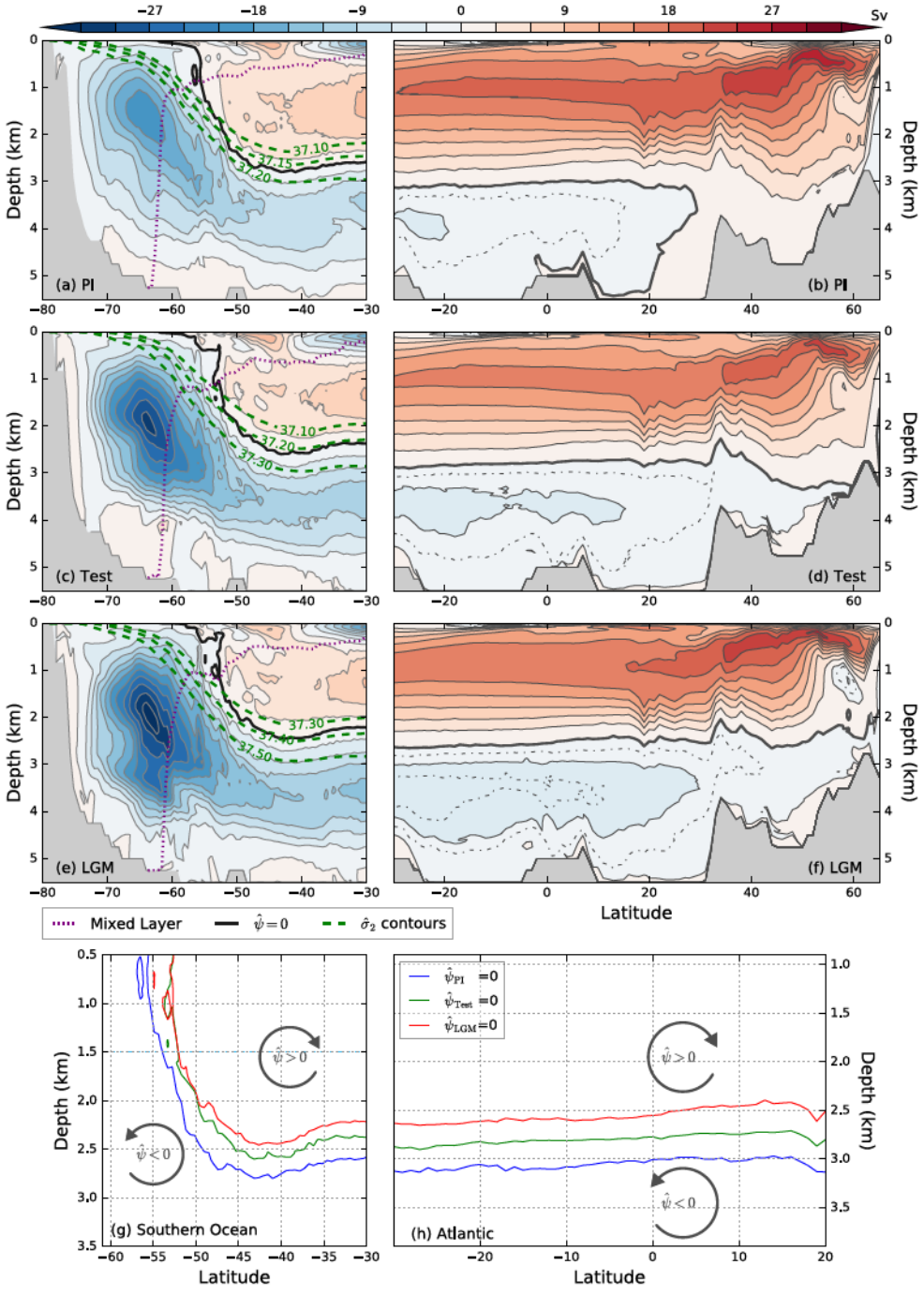

Figure S5. As in Figure 1 of the main text, but using un-smoothed data in the Southern Ocean.

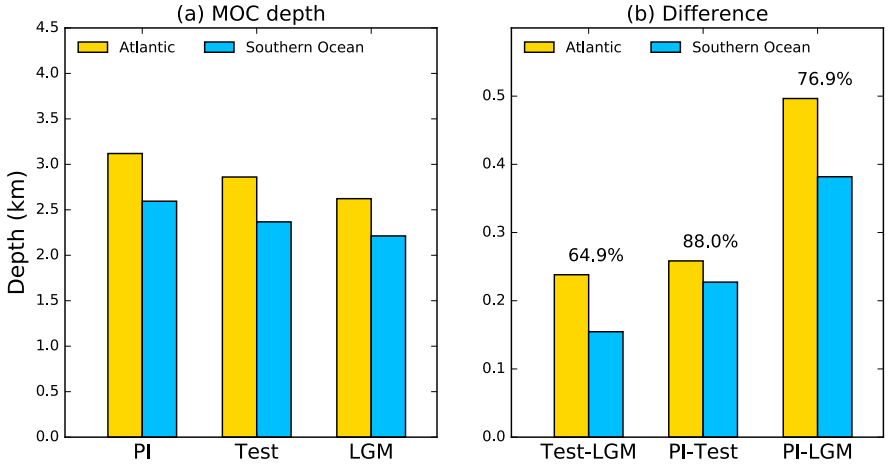

Figure S6. (a) MOC depth in Atlantic and in the Southern Ocean at 30°S and (b) comparison of the MOC depth between the three simulations. The percentage in panel (b) shows the ratio between the MOC depth differences in the Southern Ocean vs that in the Atlantic Ocean. This implies that the AMOC depth changes can be mostly attributed to the MOC changes in the Southern Ocean in our simulations. The lower percentage for "Test-LGM" and "PI-LGM" in (b) implies the importance of the North Atlantic processes in modifying the inter-basin transport of NADW between the Atlantic ocean and the Pacific ocean, which will be discussed in a later study.

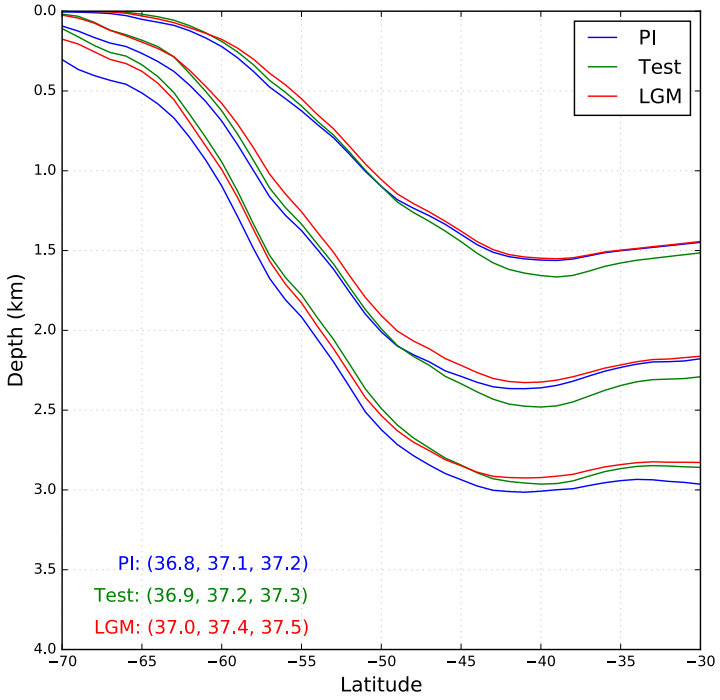

Figure S7. Contours of $\hat{\sigma}_2(y, z)$ to compare the isopycnal slopes between the three simulations. The potential densities for the three plotted isopcynals (from top to bottom) in each simulation are provided in the bottom left in units of kg/m^3.

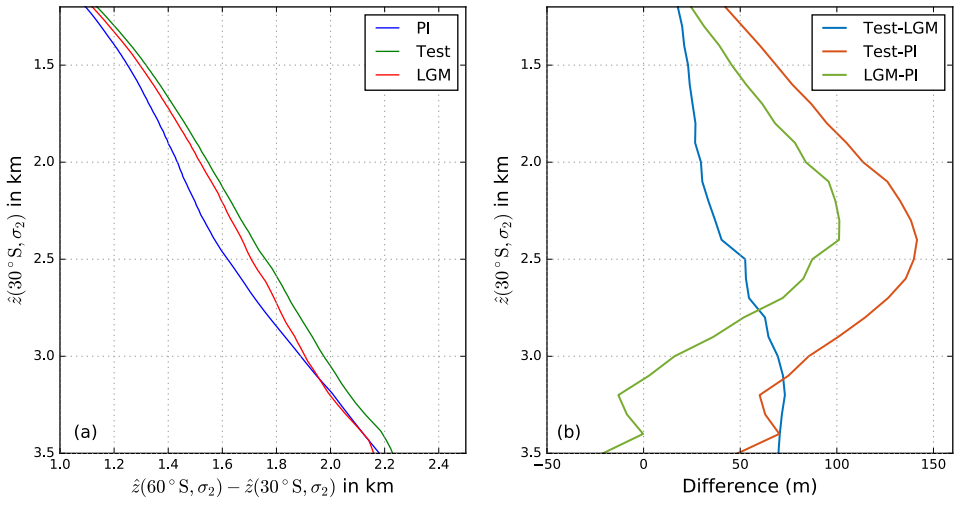

Figure S8. (a) Depth change of isopcynals $\Delta\hat{z}$ from 60°S to 30°S. (b) Difference in $\Delta\hat{z}$ between the three simulations.

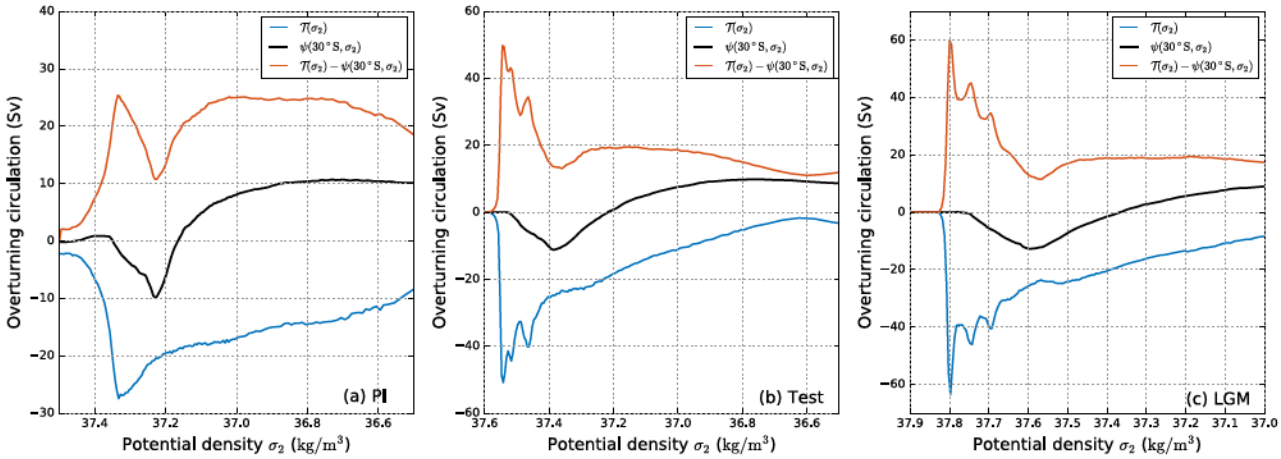

Figure S9. Water mass transformation due to surface buoyancy flux (blue lines), overturning circulation at 30°S (black lines), and the residual that is due to diapycnal transport (red lines). This is not sensitive to the reference pressure, i.e., the strong diapycnal transformation is similar if calculated using σ_0 or σ_4 coordinates.

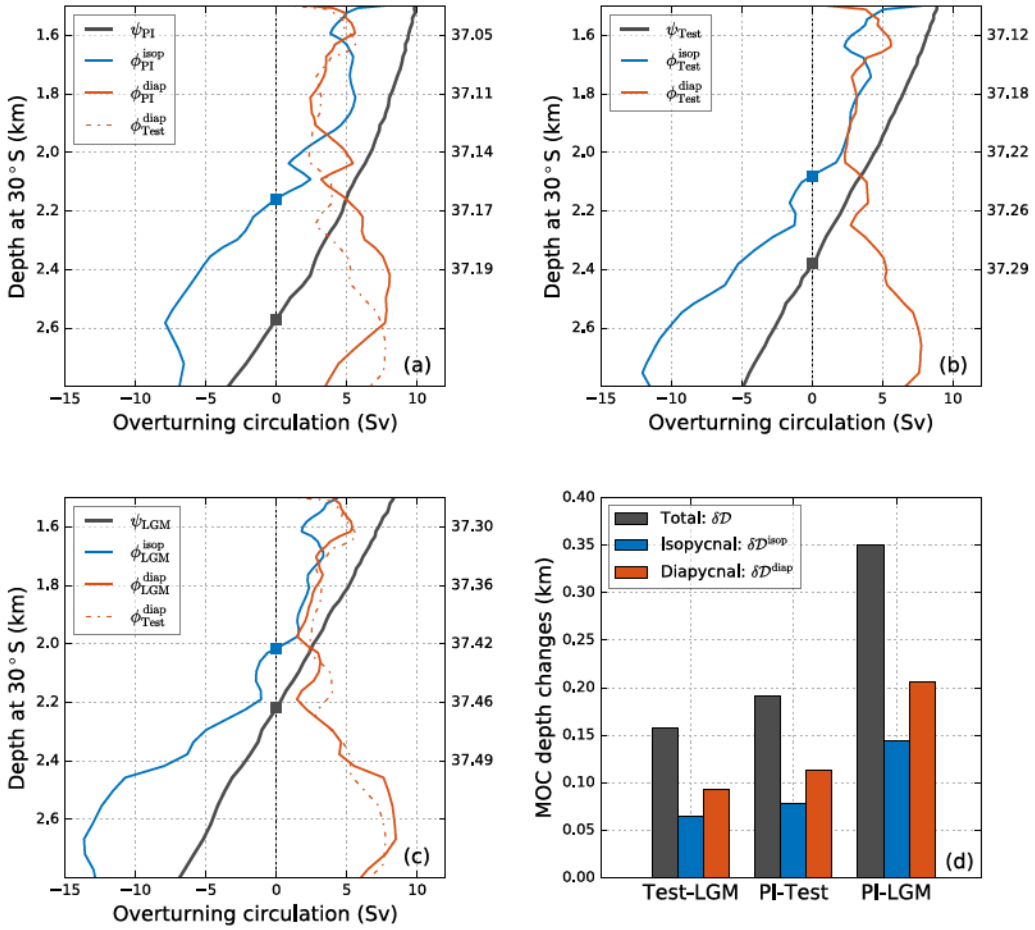

Figure S10. As in Figure 2 of the main text, but using un-smoothed data in the Southern Ocean.

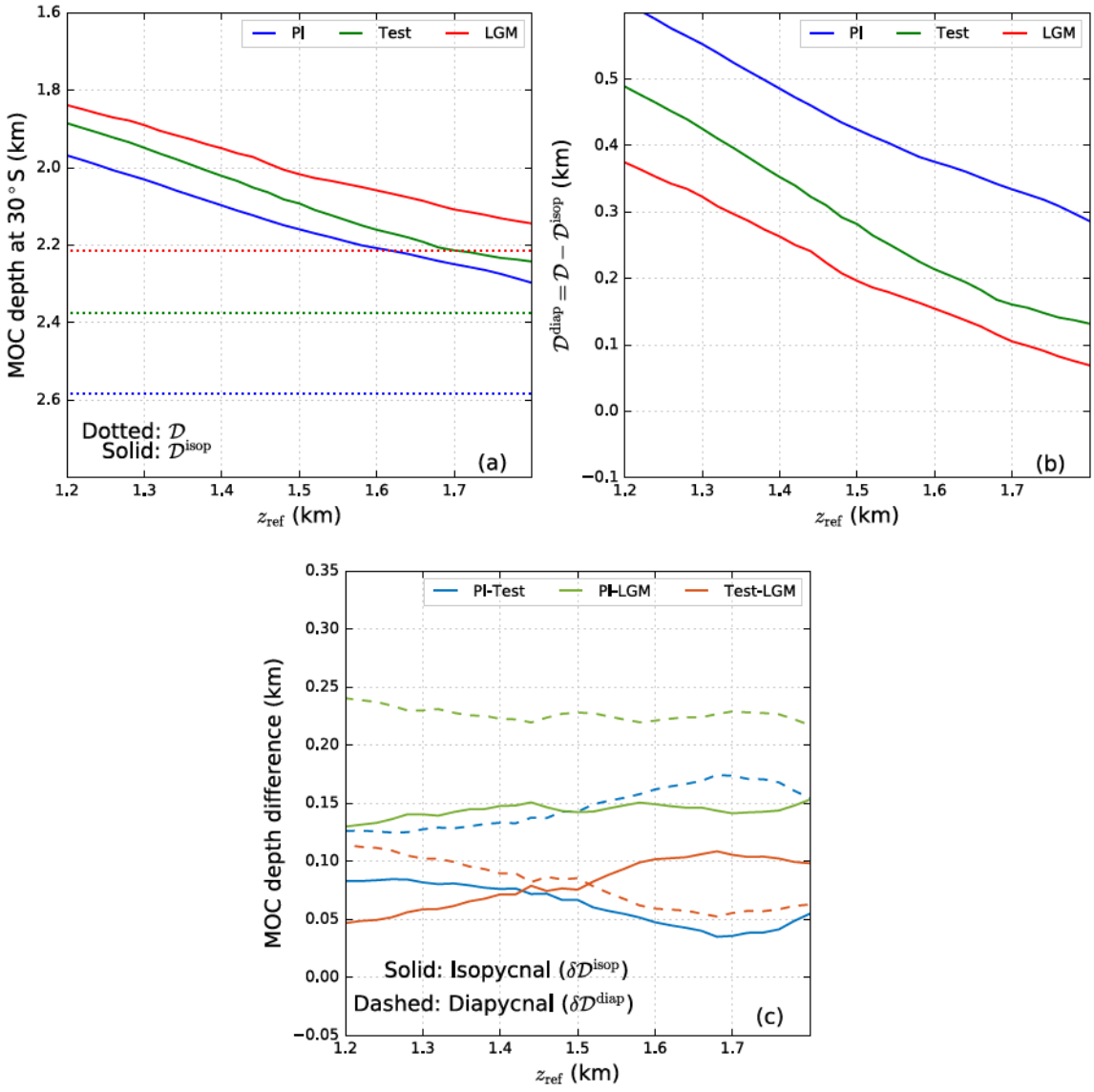

Figure S11. Dependence of $\mathcal{D}$ (a), $\mathcal{D}^{\mathrm{isop}}$ (a), $\mathcal{D}^{\mathrm{diap}}$ (b), $\delta\mathcal{D}^{\mathrm{isop}}$, and $\delta\mathcal{D}^{\mathrm{diap}}$ on the reference depth z_{ref} as discussed in Section 4. The y-axis is reversed in (a) to show that higher $\mathcal{D}$ means deeper depth. The contribution of diapycnal mixing to the MOC depth ($\mathcal{D}^{\mathrm{diap}}$) decreases with the reference depth because the integral area (represented by L_y in Figure 3) is smaller for larger z_{ref}. However, the contribution of diapycnal mixing to the MOC depth difference is insensitive to the reference depth.

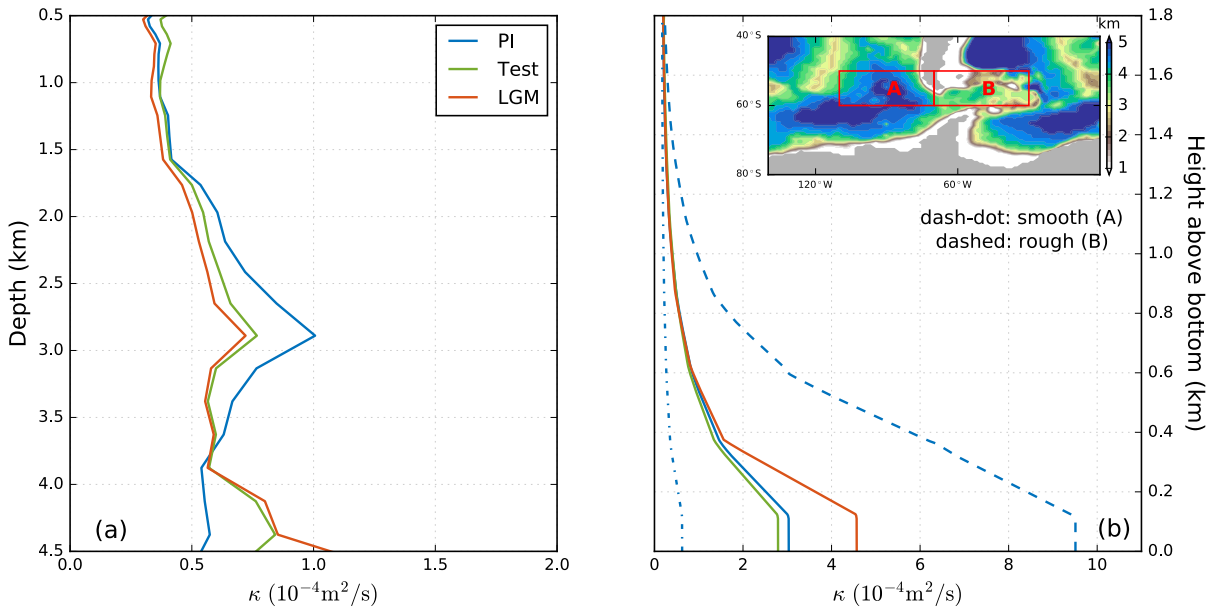

Figure S12. Diapycnal diffusivity averaged on constant depth (a) and on constant height above bottom topography (b) between 60°S and 30°S. Deep convection regions ($\kappa \approx 1\text{m}^2/\text{s}$) are excluded. In Panel (b), only regions deeper than 2000m are considered following *Waterhouse et al.* [2014]. This explains why diapycnal diffusivity is the largest in the PI run in Panel (a) between 1.5km and 3.5 km depth, due to its weak stratification, but it is not seen in Panel (b). The subplot within Panel (b) shows the bathymetry (km) close to the Drake passage. To compare with observations, we calculate the mean diapycnal diffusivity profiles over smooth topography (dash-dotted lines; A) and rough topography (dashed lines; B) close to the Drake passage for the PI simulation. And we find that both diapycnal diffusivity profiles are within the observed range given by *Waterhouse et al.* [2014]. The regions denoted by "A" and "B" correspond approximately to the domain of the DIMES project, where *Mashayek et al.* [2017] concludes the diapycnal mixing to be $O(10^{-4})\text{m}^2/\text{s}$ at 1500m depth. We averaged the diapycnal diffusivity at 1500m depth over the region denoted by "A" and "B", and we find a diapycnal diffusivity of $1.4\times10^{-4}\text{m}^2/\text{s}$, consistent with *Watson et al.* [2013].

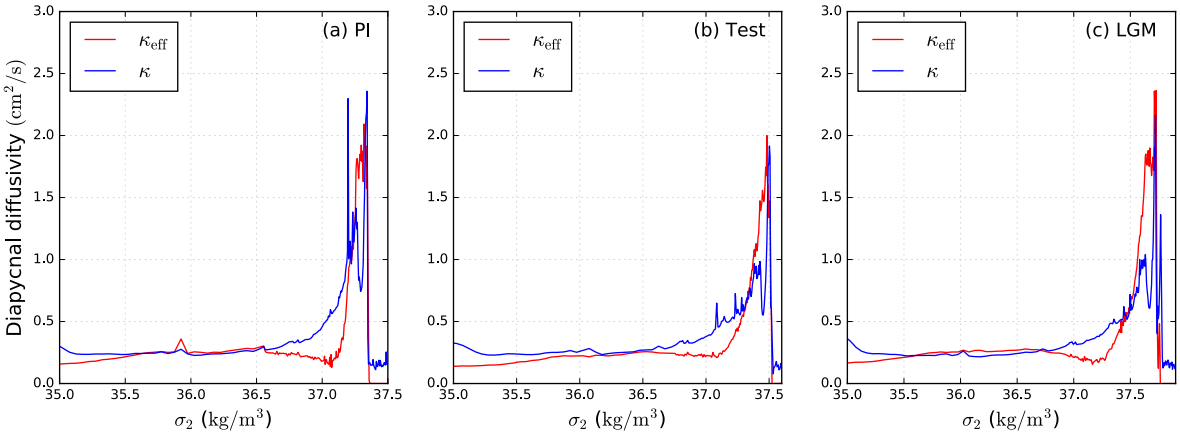

Figure S13. Effective diapycnal diffusivity (κ_{eff}, defined in Equation (S4)) and model-reported diapycnal diffusivity (κ, defined in Equation (S5)) calculated between 30°S and 30°N. The potential density range covers the depth range from intermediate depth to the ocean bottom.

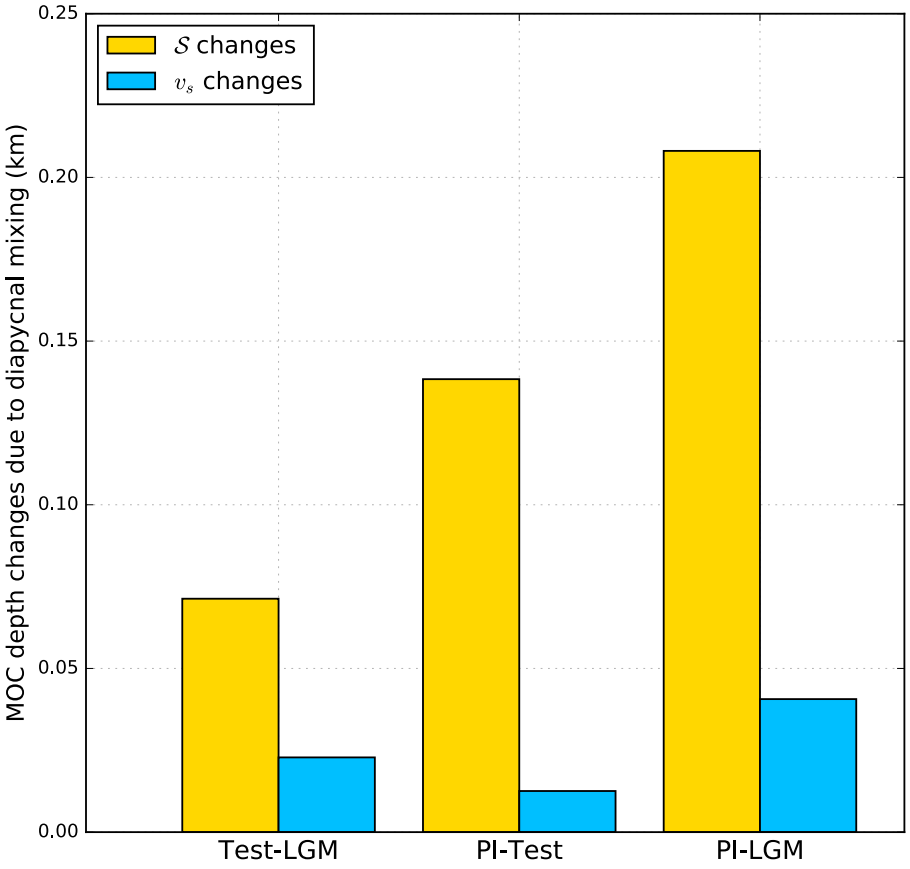

Figure S14. Contribution of diapycnal mixng to MOC depth changes due to changes in $\mathcal{S}$ and v_s according to Equation (9).

References

Böning, C. W., A. Dispert, M. Visbeck, S. Rintoul, and F. U. Schwarzkopf (2008), The response of the Antarctic Circumpolar Current to recent climate change, *Nat. Geosci.*, *1*(12), 864–869.

Brady, E. C., B. L. Otto-Bliesner, J. E. Kay, and N. Rosenbloom (2013), Sensitivity to glacial forcing in the CCSM4, *J. Clim.*, *26*(6), 1901–1925.

Ferrari, R., M. F. Jansen, J. F. Adkins, A. Burke, A. L. Stewart, and A. F. Thompson (2014), Antarctic sea ice control on ocean circulation in present and glacial climates, *Proc. Natl. Acad. Sci.*, *111*(24), 8753–8758.

Gent, P. R., and G. Danabasoglu (2011), Response to increasing Southern Hemisphere winds in CCSM4, *J. Clim.*, *24*(19), 4992–4998.

Gent, P. R., and J. C. Mcwilliams (1990), Isopycnal mixing in ocean circulation models, *J. Phys. Oceanogr.*, *20*(1), 150–155.

Gent, P. R., G. Danabasoglu, L. J. Donner, M. M. Holland, E. C. Hunke, S. R. Jayne, D. M. Lawrence, R. B. Neale, P. J. Rasch, M. Vertenstein, et al. (2011), The community climate system model version 4, *J. Clim.*, *24*(19), 4973–4991.

Griffies, S. M., R. C. Pacanowski, and R. W. Hallberg (2000), Spurious diapycnal mixing associated with advection in az-coordinate ocean model, *Mon. Weather Rev.*, *128*(3), 538–564.

Hill, C., D. Ferreira, J.-M. Campin, J. Marshall, R. Abernathey, and N. Barrier (2012), Controlling spurious diapycnal mixing in eddy-resolving height-coordinate ocean models–insights from virtual deliberate tracer release experiments, *Ocean Modell.*, *45*, 14–26.

Jayne, S. R. (2009), The impact of abyssal mixing parameterizations in an ocean general circulation model, *J. Phys. Oceanogr.*, *39*(7), 1756–1775.

Large, W. G., J. C. McWilliams, and S. C. Doney (1994), Oceanic vertical mixing: A review and a model with a nonlocal boundary layer parameterization, *Rev. Geophys.*, *32*(4), 363–403.

Marzocchi, A., and M. F. Jansen (2017), Connecting Antarctic sea ice to deep-ocean circulation in modern and glacial climate simulations, *Geophys. Res. Lett.*, *44*(12), 6286–6295.

Mashayek, A., R. Ferrari, S. Merrifield, J. R. Ledwell, L. St Laurent, and A. Naveira Garabato (2017), Topographic enhancement of vertical turbulent mixing in the Southern Ocean, *Nat. Communi.*, *8*, 14,197.

Mazloff, M. R., P. Heimbach, and C. Wunsch (2010), An eddy-permitting Southern Ocean state estimate, *J. Phys. Oceanogr.*, *40*(5), 880–899.

Munk, W. H. (1966), Abyssal recipes, in *Deep-Sea Res.*, vol. 13, pp. 707–730, Elsevier.

Newsom, E. R., C. M. Bitz, F. O. Bryan, R. Abernathey, and P. R. Gent (2016), Southern Ocean deep circulation and heat uptake in a high-resolution climate model, *J. Clim.*, *29*(7), 2597–2619.

Sun, S., I. Eisenman, and A. L. Stewart (2016), The influence of southern ocean surface buoyancy forcing on glacial-interglacial changes in the global deep ocean stratification, *Geophys. Res. Lett.*, *43*(15), 8124–8132.

Viebahn, J., and C. Eden (2010), Towards the impact of eddies on the response of the Southern Ocean to climate change, *Ocean Modell.*, *34*(3), 150–165.

Walin, G. (1982), On the relation between sea-surface heat flow and thermal circulation in the ocean, *Tellus*, *34*(2), 187–195.

Waterhouse, A. F., J. A. MacKinnon, J. D. Nash, M. H. Alford, E. Kunze, H. L. Simmons, K. L. Polzin, L. C. St. Laurent, O. M. Sun, R. Pinkel, et al. (2014), Global patterns of diapycnal mixing from measurements of the turbulent dissipation rate, *J. Phys. Oceanogr.*, *44*(7), 1854–1872.

Watson, A. J., J. R. Ledwell, M.-J. Messias, B. A. King, N. Mackay, M. P. Meredith, B. Mills, and A. C. Naveira Garabato (2013), Rapid cross-density ocean mixing at mid-

depths in the Drake Passage measured by tracer release, *Nature*, *501*(7467), 408.

Wolfe, C. L., and P. Cessi (2010), What sets the strength of the middepth stratification and overturning circulation in eddying ocean models?, *J. Phys. Oceanogr.*, *40*(7), 1520–1538.

Zhang, X., G. Lohmann, G. Knorr, and X. Xu (2013), Different ocean states and transient characteristics in Last Glacial Maximum simulations and implications for deglaciation, *Clim. Past*, *9*(5), 2319.